Materials and Structures (2026) 59:183
https://doi.org/10.1617/s11527-026-03084-7

ORIGINAL ARTICLE

Effect of aggregate shape representation and deformability on the bituminous mixture stiffness properties using 3D DEM modelling

R. Micaelo · N. Monteiro Azevedo · G. Câmara

Received: 26 November 2025 / Revised: 11 March 2026 / Accepted: 1 April 2026 / Published online: 9 April 2026

Abstract Given the recognised importance of aggregate shape in the performance of bituminous mixtures, there has been growing interest in developing numerical models that accurately capture the material's mesostructural characteristics. This paper presents a methodology for incorporating complex aggregate shapes into three-dimensional (3D) Discrete Element Method (DEM) models of bituminous materials and investigates the impact of representing coarse aggregates as deformable bodies on both the geometry and mechanical response of DEM assemblies. This approach was implemented in VirtualPM-3DLab, a 3D DEM software that employs Laguerre–Voronoi diagrams to define spherical particle contacts and contact areas, together with a generalised Kelvin contact model to simulate the viscoelastic behaviour of bituminous materials. The mechanical response of DEM assemblies, using rigid single-spherical particle aggregates versus deformable multi-spherical particle aggregates, was analysed through simulated uniaxial tension–compression cyclic tests at various frequencies. The results show that discretising the aggregate volume using a distribution of smaller-radius spherical particles effectively captures aggregate geometry, although the sphere size distribution must be carefully selected to ensure high-fidelity representation. Virtual asphalt specimens with deformable multi-sphere aggregate particles exhibited higher stiffness moduli and lower phase angles across the tested frequencies compared to rigid single-sphere specimens. These variations in viscoelastic properties were more pronounced with finer aggregate discretisation, due to the increased number of aggregate–aggregate and aggregate–mastic contacts. In contrast, the total number of contacts and their distribution among constituents were very similar for assemblies with irregular particle models (realistic) and subdivided icosahedron models (close to spherical), resulting in a minimal effect of aggregate shape on the overall DEM simulation results.

Keywords Discrete element method · Bituminous mixture · Image processing techniques · Aggregate shape · Aggregate deformability · Viscoelasticity

R. Micaelo (✉)
CERIS, Department of Civil Engineering, NOVA School of Science and Technology (NOVA FCT), NOVA University Lisbon, Caparica, Portugal
e-mail: ruilbm@fct.unl.pt

N. Monteiro Azevedo · G. Câmara
LNEC – National Laboratory for Civil Engineering, Av. do Brasil 101, 1700-066 Lisbon, Portugal
e-mail: nazevedo@lnec.pt

G. Câmara
e-mail: gcamara@lnec.pt

1 Introduction

Bituminous mixture, or asphalt in the European terminology, is the most used material for road surfacing

due to its superior performance relative to the life-cycle cost and comfort to road users, and due to the fact that it can be recycled multiple times with small input of energy and new raw materials depending of the technique adopted [1, 2]. The bituminous mixture is conventionally composed of approximately 90% aggregates and 10% bitumen by volume ratio, and both component's properties significantly affect the production and in-service performance of the mixture. Thus, the mixture is designed, following an extensive laboratory procedure (e.g., European standard EN 13108-1:2016 to asphalt concrete [3]), with a precise combination of several aggregate fractions and bitumen to achieve a densely packed internal structure, meeting the mechanical and performance testing requirements. The process is repeated when using different aggregates and bitumen, or when introducing a new constituent, such as reclaimed asphalt or fibres. This approach is not resource and time efficient which limits the innovation and acceptation of new designs by industry. Numerical approaches, especially the ones that can explain the behaviour of composite materials from the constituents' properties offer an outstanding opportunity to the referred challenge.

The Discrete Element Method (DEM) is one method that has been largely implemented to model bituminous mixtures at the micromechanical level [4]. The discontinuous medium formed by different sized aggregates, bitumen and additives is discretised with discrete elements, with their contacts represented by defined constitutive models. Hence, the DEM model can represent the loading transmission mechanisms within the material and the formation of discontinuities (cracks), enabling the explanation of failure and performance across different material designs [5–8]. In the past, two-dimensional (2D) DEM models were exclusively used due to the high computational demand of simulations. For instance, You [9] developed one of the first 2D DEM studies of bituminous mixtures, aiming to predict stiffness properties under various testing conditions. Despite discretising individual aggregates with a collection of small circular particles to better represent particle shapes, the model was found to underestimate the stiffness for mixtures where aggregate-aggregate contacts were less perceptible in specimen photographs. Thus, the inter-particle aggregate contact network is a true three-dimensional (3D) structure that cannot be fully described from the surface of sawn specimens. Lira et al. [10] used a numerical procedure based on 3D packing theory to evaluate the effect of the shape and size distribution of the aggregate mixture on the structure of the material and, indirectly, on the stability and rutting resistance.

To overcome known DEM computation time limitations, Liu and You [11] showed that it is possible to accelerate 3D asphalt DEM models with aggregate and mastic discretisation by increasing the loading frequency according to the frequency-temperature superposition principle. In the last decade, the use of 3D DEM models for the investigation of bituminous mixtures has become common. For example, Liu et al. [12] studied the displacement of aggregates during the laboratory static compaction process of asphalt specimens; Nian et al. [13] studied the anti-cracking performance of asphalt when subjected to indirect tension of cylindrical specimens and three-point flexural bending of beam specimens at temperatures ranging from -15 ºC to 15 ºC; Câmara et al. [14] modelled mastic and asphalt prismatic specimens under uniaxial cyclic tension–compression loading; and Peng et al. [15] analysed the effect of asphalt specimen composition on shear fatigue performance by modelling different cylindrical specimens subjected to repeated uniaxial penetration tests. A comprehensive literature review on the use of DEM to investigate asphalt behaviour can be found in [4].

Often, DEM assemblies use circular particles in 2D or spherical particles in 3D to simulate aggregates, which fail to capture the effects of shape and texture. Various approaches have been proposed in the literature [16–20] to build complex particle morphologies in DEM assemblies. For example, Ma et al. [21] generated a dense packing of small spheres arranged in a regular pattern, then defined coarse aggregate particles as rigid clusters consisting of the spheres located within a target volume obtained by intersecting a larger virtual sphere with several cutting planes. In [16], individual aggregates were measured with an X-ray Computed Tomography (CT) system to create triangulated surface models. The aggregate shape models were filled with small spheres, placed in a designated space and compacted using gravity and wall movement, resulting in a tightly packed assembly. Valera et al. [17] defined realistic particle morphologies using Fourier descriptors, and then the assembly was constructed by merging advancing front techniques with dynamic methods. Finally,

the particles are replaced with clusters of spheres to perform DEM simulations. Mollon and Zhao [18] proposed a method to generate complex and controllable shapes based on the theory of random fields and a Fourier shape descriptor. To build the assembly, the virtual aggregates are inserted in the volume with a defined cell-filling algorithm based on the constrained Voronoi tessellation method. The authors did not perform DEM simulations but suggested replacing individual aggregates with overlapping spheres. Similarly, Garcia-Hernandez et al. [22] used a physics engine software (Unity 3D) to create virtual aggregates and compacted assemblies. The starting volumetric element (prism) goes through a sequence of mathematical procedures to obtain a complex shape and those that match the 50% probability values of the perimeter and surface area are kept for later use. The individual aggregates are inserted floating in a large container and then compacted by gravity and wall displacement.

Therefore, representing aggregates with realistic morphologies in the DEM model commonly involves three main steps: (1) the aggregate shapes must be numerically/mathematically defined; (2) these defined shapes must be used to construct the aggregates within the DEM framework; and (3) building a compacted assembly with particle-to-particle contacts. Steps (2) and (3) can also be implemented in the reverse order. In practice, the aggregates morphologies are often simplified in the numerical model to reduce computation time and effort, which may compromise both the accuracy and efficiency of simulations. To investigate this trade-off, Wei et al. [23] evaluated the influence of aggregate shape detail, defined by number of facets in the triangular surface mesh, on the mechanical response and computational time of a finite element (FE) model. Their results showed that the most simplified aggregate representations led to significant deviations from experimental observations. However, at an intermediate resolution of 100 facets, the numerical response was comparable to that of the most detailed model, while requiring only about half the computational time.

In addition, the influence of complex aggregate geometries on the response of 3D numerical models remains insufficiently explored, although existing studies highlight their relevance. For example, Gong et al. [24] investigated the effect of aggregate shapes on thermo-mechanical properties using a 3D FE model. They reported that incorporating more complex, numerically defined shapes derived from regular geometries, led to higher stiffness moduli compared with spherical and ellipsoidal aggregates, with the effect becoming more pronounced at higher temperatures and loading frequencies. In contrast, the variation in phase angle across different shape models was small. Similarly, Kusumawardani and Wong [25] analysed the mechanical response of a 3D DEM model of porous asphalt in which coarse aggregates were represented as cubes, cylinders and spheres. They observed substantial differences in properties among assemblies, along with a strong relationship between aggregate shape and bulk skeleton strength, which was attributed to the degree of effective particle contact.

In summary, the recognised importance of aggregate shape in the performance of bituminous mixtures has motivated efforts to develop numerical models that more accurately capture the material's mesostructure. In a previous study [14], the authors developed a 3D DEM tool (VirtualPM3DLab) to model asphalt materials at the mesostructural level, explicitly representing aggregates and mastic while adopting strategies to reduce the associated computational cost. VirtualPM3DLab also incorporates an innovative 3D generalised Kelvin contact model, formulated incrementally for nonlinear analysis, which enables the viscoelastic behaviour of bituminous materials to be captured under different temperature and frequency conditions.

The software employs Laguerre–Voronoi diagrams to define inter-particle contacts and contact areas within an initially spherical particle assembly, approximating the domain as an assembly of polyhedral particle shapes while retaining the contact handling simplicity of spheres interactions. This approach provides both computational efficiency and a realistic contact network. However, the assumption that larger aggregates are rigid and approximately spherical may limit the ability to achieve a realistic mesoscopic representation of bituminous materials.

In the present work, the VirtualPM3DLab is enhanced by incorporating realistic aggregate geometries through a digital library of shapes obtained from X-ray computed tomography. Aggregate deformability is introduced by adopting an internal discretisation using small spherical particles. These developments enable the evaluation of the influence of aggregate

shape and deformability on volumetric properties and on the macroscopic response under uniaxial tension–compression cyclic loading.

2 Objectives and scope

The main objectives of this paper are to present a methodology for incorporating complex aggregates shapes into DEM models of bituminous materials and to analyse the effect of representing coarse aggregates as deformable bodies on both the geometry and on the mechanical response of DEM assemblies.

The proposed methodology involves constructing a digital library of aggregate shapes and modelling the selected shapes in the numerical assembly using clusters of small spherical particles, whose deformability is determined by the contacts between these internal particles. The shapes included in the digital library were extracted from X-ray computed tomography scans of bituminous mixtures and processed using an adaptive image-processing procedure combined with the Delaunay method to generate 3D surface models of the aggregates. This aggregate representation method was integrated in VirtualPM3DLab, a 3D DEM software program [14].

Compared with other complex-shape generation approaches, such as those relying on background assemblies of small spherical particles arranged in a regular pattern [12, 21], the proposed method provides a more realistic representation of aggregate surfaces through internal discretisation and Voronoi-based shapes. It also removes the directional mesh bias inherent to regular grids and incorporates a random particle-size distribution for the mastic.

The mechanical response of DEM assemblies incorporating deformable multi-sphere clusters representing coarse aggregates is evaluated through simulated uniaxial tension–compression cyclic tests performed at various frequencies. The macroscopic response of these assemblies is compared with that of rigid single-sphere aggregate models. Several aggregate shape configurations were considered to separately investigate the effects of aggregate deformability and aggregate morphology. These two aspects are relevant and largely absent in the existing literature. The influence of the internal particle size used for aggregate discretisation is also evaluated, given its substantial impact on the associated computational cost.

3 3D DEM model based on Laguerre–Voronoi tessellation

3.1 Fundamentals/Voronoi-generalised contact model

The VirtualPM3DLab is a DEM based tool programmed in C++ that uses a 3D generalised contact model explicit formulation applied to spherical particles [14]. The numerical method relies on two main principles [26]: (1) the forces exerted on each particle are linked to its relative displacements with respect to neighbouring particles, considering the applied forces; and (2) Newton's laws of motion are used to determine the updated positions of the particles. At each computational step, the applied forces on each particle are used to compute their new positions and velocities based on Newton's second law. The equations of motion for a spherical particle, at time t, can be expressed as follows:

$$F_i(t) + Fd_i(t) = m\ddot{x}_i(t) \tag{1}$$

$$M_i(t) + Md_i(t) = I\dot{\omega}_i(t) \tag{2}$$

where, $F_i(t)$ and $Fd_i(t)$ are the total and damping forces, $M_i(t)$ and $Md_i(t)$ are the total and damping momenta, $\ddot{x}_i(t)$ and $\dot{\omega}_i(t)$ are the linear and angular accelerations, and m and I are the mass and inertia of particle.

The VirtualPM3DLab uses the Laguerre–Voronoi diagrams to establish the particle contacts and the contact areas [27, 28]. In this approach, each spherical particle is assigned a polyhedral shape based on the weighted Delaunay tetrahedralisation of the gravity centres of the spherical particles. The facets of the resulting polyhedral shapes are equidistant to the gravity centre of the corresponding polyhedron and are shared with neighbouring particles' polyhedral shapes. It is noteworthy to mention that while the Laguerre–Voronoi facets are close to the contact locations defined by the single point contact method, the gravity centre of the polyhedral shape does not necessarily coincide with that of the traditional single point contact plane. Hence, this methodology approximates the domain as

an assembly of polyhedral particle shapes while retaining the geometric simplicity of spherical particles and ensuring low computational costs.

In the VirtualPM3DLab, the force ($F_i^{[C]}$) and moment ($M_i^{[C]}$) resulting from the contact C between two spheres are defined given the contribution of the forces ($F_i^{[J]}$) acting at local points ($J=1$ to N) at the Laguerre–Voronoi facet associated with that contact, shown in Fig. 1c, as:

$$F_i^{[C]} = \sum_{J=1}^{N} F_i^{[J]} \tag{3}$$

$$M_i^{[C]} = -\sum_{J=1}^{N} e_{ijk}\left(x_i^{[J]} - x_i^{[0]}\right)F_i^{[J]} \tag{4}$$

where, e_{ijk} is the permutation tensor, $x_i^{[J]}$ are the positions of the contact points at the Laguerre–Voronoi facet, and $x_i^{[0]}$ is the contact reference point position.

The contact reference point position is initially defined at the intersection of the line connecting the spheres centres with the Laguerre–Voronoi facet (see Fig. 1b), and then updated during the simulation as:

$$x_i^{[0]} = x_i^{[A]} + \left(R^{[A]} - \frac{1}{2}Un - dv\right)n_i \tag{5}$$

where, $x_i^{[A]}$ and $R^{[A]}$ are the centre position and radius, respectively, of sphere A; n_i is the unit normal of the direction line between the centres of spheres A and B; dv is the distance between the initial position of the Laguerre–Voronoi facet and the contact location using the single point contact method; and Un is the contact overlap,

$$Un = R^{[A]} + R^{[B]} - d \tag{6}$$

where, d is the distance between the centres of spheres A and B. To determine the global positions of the contact points in the facet is used a local reference system (s_i, t_i), centred at $x_i^{[0]}$, with the axes defined such that $\vec{s}\times\vec{t} = \vec{n}$. Hence, the contact points are determined during the simulation from the local coordinates $\left(s^{[J]}, t^{[J]}\right)$ that are defined given the Voronoi facet:

$$x_i^{[J]} = x_i^{[0]} + s^{[J]}s_i + t^{[J]}t_i \tag{7}$$

and the displacement velocity of particle A relative to particle B at the local contact point ($\dot{x}_i^{[J]}$) is calculated as:

$$\dot{x}_i^{[J]} = \dot{x}_i^{[A,J]} - \dot{x}_i^{[B,J]} = \left(\dot{x}_i^{[B]} + e_{ijk}\omega_j^{[B]}\left(x_k^{[J]} - x_k^{[B]}\right)\right) - \left(\dot{x}_j^{[A]} + e_{ijk}\omega_j^{[A]}\left(x_k^{[J]} - x_k^{[A]}\right)\right) \tag{8}$$

The forces at the contact points are decomposed in two components, normal and shear, and follow an incremental linear law during the simulation, however, the calculation procedure varies with the contact model.

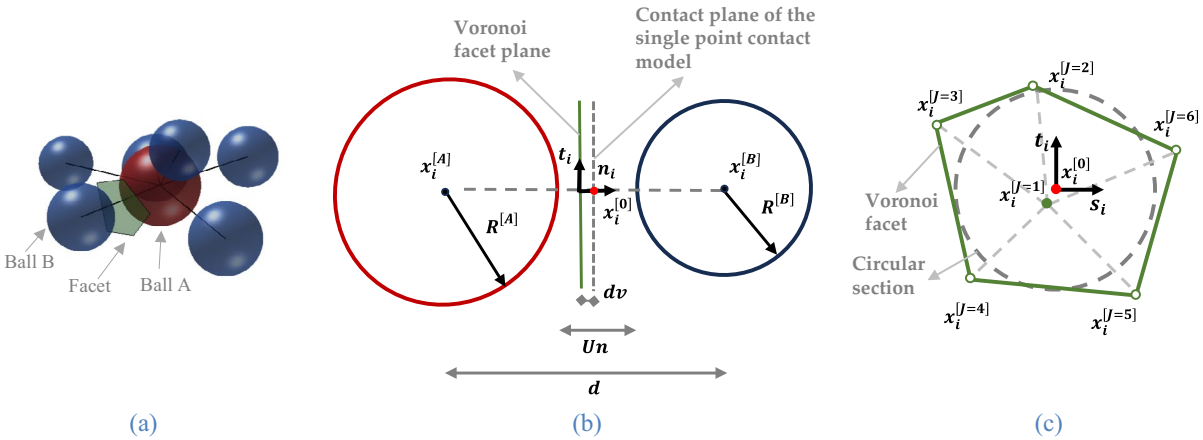

Fig. 1 VirtualPM3DLab contact model: **a** 3D perspective; **b** (t, n) plane; **c** (t, s) plane

3.1.1 Linear elastic model

The force increments at the local contact points, associated with a linear elastic contact model, in a DEM cycle are calculated as:

$$\Delta F_i^{[J,n]} = -kn^{[J]}\Delta x^{[J,n]} = -kn^{[J]}\left(\dot{x}_i^{[J]}\Delta t\right)n_i \tag{9}$$

$$\Delta F_i^{[J,s]} = -ks^{[J]}\Delta x_j^{[J,s]} = -ks^{[J]}\left(\dot{x}_i^{[J]}\Delta t\right) - \Delta x^{[J,n]}n_i \tag{10}$$

where,$kn^{[J]}$ and $ks^{[J]}$ are the normal and shear contact stiffnesses, $\Delta x^{[J,n]}$ is the contact displacement (scalar) in the normal direction, and $\Delta x_i^{[J,s]}$ is the contact displacement (vector) in the shear direction, Δt the calculation timestep, and $\dot{x}_i^{[J]}$ is the relative contact velocity. In VirtualPM3DLab, the normal and shear contact stiffnesses at the local contact point are calculated as:

$$kn^{[J]} = \frac{\overline{E}}{d}A^{[J]}\delta \tag{11}$$

$$ks^{[J]} = \alpha kn^{[J]} \tag{12}$$

where, $\overline{E}$ is the elastic modulus of the equivalent continuum material, d is the distance between the particles centre of gravity, $A^{[J]}$ is the contact area, α is the ratio between the normal and shear stiffnesses, and δ is the calibration coefficient between the macroscopic and mesoscopic properties. The contact area associated with the contact point is obtained by summing one third of the area of the triangles containing the point (see Fig. 1b).

3.1.2 Linear viscoelastic contact model–generalised Kelvin model

In VirtualPM3DLab, the viscoelastic behaviour of bituminous materials is represented using the generalised Kelvin (GK) contact model, which consists of one Maxwell model unit in series with multiple Kelvin model units (see Fig. 2). The GK model was implemented in VirtualPM3DLab, where the constitutive equations are integrated using a time-centred difference method as proposed by Câmara et al. [14]. The force increment in the normal direction at the local point J, during a DEM computational cycle, is calculated as:

$$\Delta F^{[J,n]}(\Delta t) = \frac{1}{c}\left[\Delta x^{[J,n]}(\Delta t) + \sum_l\left[\Delta x_{ve,l}^{[J,n]}(t)\left(1-\frac{b_l}{a_l}\right)\right]\right] - \left(1+\frac{g}{c}\right)F^{[J,n]}(t) \tag{13}$$

where, $\Delta x^{[J,n]}(\Delta t)$ is the total displacement increment in the normal direction at the local point J, and $\Delta x_{ve,l}^{[J,n]}(t)$ is the accumulated viscoelastic displacement in the normal direction at the local point J in the l^{th} Kelvin element at time t that is obtained as:

$$\Delta x_{ve,l}^{[J,n]}(t) = \frac{1}{a_l}\left[b_l\Delta x_{ve,l}^{[J,n]}(t-\Delta t) + \frac{\Delta t\left[F^{[J,n]}(t) - F^{[J,n]}(t-\Delta t)\right]}{2\eta_l}\right] \tag{14}$$

and constants a_l, b_l, c and g are:

$$\begin{cases} a_l = 1 + \frac{k_l\Delta t}{2\eta_l} \\ b_l = 1 - \frac{k_l\Delta t}{2\eta_l} \\ c = \sum_l\left(\frac{\Delta t}{2a_l\eta_l}\right) + \frac{1}{kn_m} + \frac{\Delta t}{2\eta_m} \\ g = \sum_l\left(\frac{\Delta t}{2a_l\eta_l}\right) - \frac{1}{kn_m} + \frac{\Delta t}{2\eta_m} \end{cases} \tag{15}$$

The formulation is the same for the normal and shear directions. The contact parameters (k and η), shown in Fig. 2, are obtained from the macro-scale GK parameters (E and C) in the same way as with the linear elastic model:

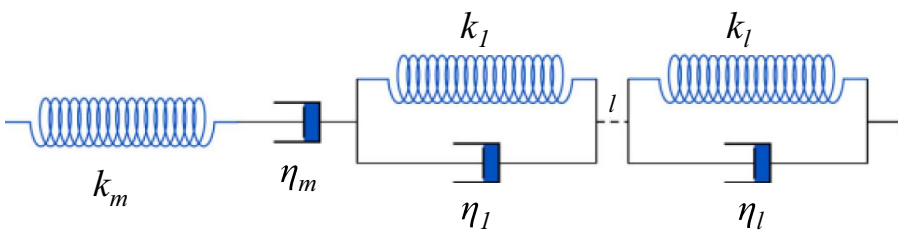

Fig. 2 Generalised Kelvin contact model

$$k_{\xi}^{[J]} = \frac{E_{\xi}}{d} A^{[J]} \delta \tag{16}$$

$$\eta_{\xi}^{[J]} = \frac{C_{\xi}}{d} A^{[J]} \delta \tag{17}$$

where, the subscript ξ corresponds to the GK unit (m for the Maxwell element, and l for the lth Kelvin element). The contact parameters in the shear direction are obtained by the product of the parameters in the normal direction and the ratio coefficient α.

3.2 Mineral aggregates representation

3.2.1 Shape model

To develop numerical models of bituminous mixtures, various methods have been used to numerically/mathematically describe the shape of individual aggregates. These methods can be classified into two categories: (1) mathematical-based methods, which create virtual aggregates with predefined geometrical properties; and (2) image-based methods, which capture the surface geometry of aggregates. In this study, an image-based method was implemented using CT scan images of a bituminous specimen. The resulting shapes were used to build a digital library for constructing DEM models.

In CT scan images of a bituminous specimen, different constituents such as the aggregate, the mastic, and the air voids, can be distinguished based on variations in pixel grey tones. This allows individual sliced images to be processed to isolate one or specific constituents, which in this study are the aggregates. The processed stack of images is then utilised to create a 3D surface model of the aggregates. The image processing procedure implemented here was adapted from the method described in [29]. It should be noted that this process differs from other techniques used to characterise individual aggregates, such as CT (e.g., [16]), laser scanning (e.g., [30]) or photogrammetry (e.g., [31]).

The sequence for processing CT scan 2D images of a bituminous sample into triangulated surface models of individual aggregates is as follows:

(1) Greyscale correction: adjustments are made to the greyscale distribution in the CT images to account for variations in brightness both across different sections and between individual images.
- Inter-image variation: pixel values are normalised by adjusting them according to the difference between the average greyscale values of each image and the overall average of the image stack.
- Intra-image variation: the greyscale distribution is analysed along the radial direction using ring zones. Pixel values are then adjusted based on the difference between the average values of the specific ring zone where the pixel is located and the image centre.

(2) Segmentation of the aggregate fraction: air voids are segmented and removed based on their greyscale values. Next, a median filter is applied to reduce noise. Finally, the aggregates are segmented from CT images using a global thresholding method, specifically the Otsu algorithm [32].
(3) Separation of touching aggregates: the separation of touching aggregates in CT images is achieved using recursive steps of erosion, fill holes, dilation and watershed algorithms.
(4) 3D model of the aggregate fraction: the stack of processed 2D images is integrated to generate a 3D triangulated surface model in STL format. A filter is applied to reduce the number of vertices and facets in the model.
(5) 3D model of individual aggregates: individual aggregate particles are extracted from the 3D model and exported as separate models. As the initial inspection to the individual models showed frequent issues, e.g., holes, the surface models were rebuilt from the point cloud using the Delaunay triangulation algorithm (TIN model). The resulting 3D surface models were measured in terms of size, surface area and volume.

These tasks were implemented with several software programs: ImageJ for CT image processing and building the 3D model of the aggregate fraction (steps 1–4); Meshlab to reduce the STL file size and export into individual models (steps 4–5); and MATLAB to build the TIN models of individual aggregates (step 5).

3.2.2 Multi-sphere inner discretisation algorithm

The individual aggregates could be readily incorporated into the VirtualPM3DLab DEM engine as

rigid polyhedral blocks [33] or as a flexible polyhedral [34, 35] by adopting an inner finite element mesh discretisation, but this would require including more complex contact detection procedures than the one's required for spherical shapes that have a lower associated computational cost. A 2D flexible particle model has been proposed by Azevedo et al. [36] that considers particle deformability by adopting in each grain, Voronoi Cell, an inner finite triangular element mesh. A hybrid DEM/FEM particle model has also been proposed in [37], where the larger particles that are expected to remain in the elastic range are discretised with finite elements. Both approaches may be developed in 3D as an extension of the VirtualPM3DLab rigid contact model, keeping the highly efficient contact detection procedures associated with spherical shapes.

Nevertheless, due to computational constraints and implementation challenges, the aggregates were represented herein using a spherical discretisation with smaller radii, similar to the approach adopted in [38]. To this end, a multi-sphere (MS) discretisation algorithm was implemented in VirtualPM3DLab to fill the internal volume of each mineral aggregate with a prescribed distribution of small spherical particles. Moreover, the aggregate deformability, which is essential for fracture studies [36, 37], is incorporated by accounting for the contact interactions, based on the Laguerre–Voronoi diagrams, between the internal spherical particles that make up each aggregate particle. Thus, each aggregate particle is a deformable cluster of small spherical particles.

Figure 3 presents for one mineral particle representation template (icosahedron theoretical template), the associated particle shape (10.0 mm diameter aggregate) and the corresponding inner particle discretisation and inner Voronoi Cells. A uniform radius distribution from 1.50 to 3.0 mm was admitted for the inner particle discretisation. When compared with the original polyhedral blocks, the aggregate representation has a higher interlock effect due to the boundary roughness. In the adopted model, the interlock effect is mitigated given that a Voronoi tessellation is adopted to establish the contacts which tends to set the contact plane closer to the initial block outer surface. The algorithm ensures that a minimum of 8 inner spherical particles can be inserted within the aggregate inner volume, otherwise a single spherical particle is adopted to represent the mineral aggregate.

3.3 Asphalt specimen generation

The adopted asphalt specimen generation procedure implemented in VirtualPM3DLab follows the principles proposed in [27, 28]. The particles representing the predefined aggregate content are inserted from the highest to the smallest diameter. The particles representing the bituminous mastic are subsequently introduced adopting a low porosity value of 0.05 and a predefined uniform radius distribution. For a given particle representing the aggregate, a template is randomly selected from the developed aggregate shape digital library that includes an additional icosahedron theoretical template. The size of the aggregate template is then adjusted to ensure that the aggregate has the desired circumscribed sphere radius within the min–max limits corresponding to the specific aggregate sieve fraction.

Prior to the aggregate insertion, the inner volume of each mineral particle is discretised with a finer particle distribution, see Sect. 3.2.2 (multi-sphere (MS) inner discretisation algorithm). The aggregate with the inner spherical particle discretisation is attempted to be inserted in the model by adopting random coordinate locations of its centre of gravity and random aggregate orientations. The particle placement ends

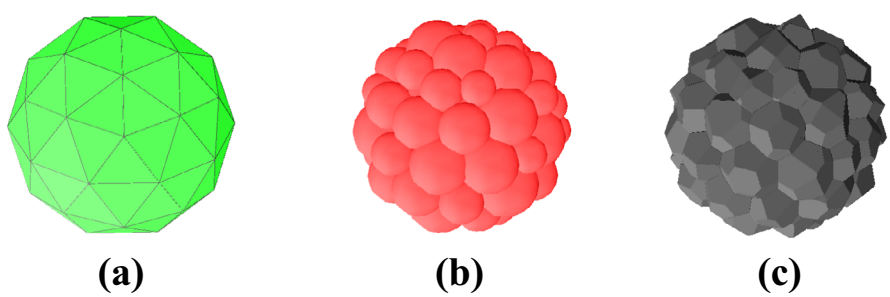

Fig. 3 Aggregate multi-sphere inner discretisation: **a** aggregate shape model; **b** inner particles; **c** Voronoi cells

when the particle representing a mineral aggregate is found not to intersect with the previously inserted particles. At the end of the particle insertion algorithm, the centres of gravity of the spherical particles are triangulated based on a weighted Delaunay algorithm and the associated Laguerre-Voronoi diagram is built from the weighted Delaunay tetrahedra structure.

Compared with existing complex-shape modelling strategies that rely on regularly arranged assemblies of small spherical particles [12, 21], the proposed approach offers enhanced fidelity in aggregate representation through internal discretisation. It also eliminates the directional bias associated with regular grids and incorporates a stochastic particle-size distribution for the mastic. Furthermore, by employing Laguerre–Voronoi diagrams to define inter-particle contacts and contact areas, the model more accurately captures the contact surface interactions, something that cannot be achieved when approximating contact areas solely using the radii of spherical particles.

4 Case study

4.1 Digital library of mineral aggregate shapes

A digital library of mineral aggregate shapes was built, with the method described in Sect. 3.2.1, using aggregates from a bituminous mixture designed for base courses, AC 20 base 40/60, which was investigated in a previous study [39]. The aggregate gradation is shown in Fig. 4, with all aggregate fractions composed of limestone. A prismatic specimen with $40 \times 40 \times 50$ mm^3 was cut from a compacted cylindrical specimen, with 100 mm of diameter and 50 mm of height, and inspected using a XRadia Versa XRM-500 scanner to characterise the inner structure. In this study, the resulting CT images were processed to obtain individual 3D surface models (TIN format) as described in Sect. 3.2.1.

A total of 82 TIN models of individual aggregates, representing different aggregate fractions of the bituminous mixture, were selected to integrate the digital library. The technical specifications for bituminous materials (e.g., NP EN 13043 [40]) require aggregate fractions to comply with several geometrical requirements, particularly dimensions and shape. To ensure compliance, the selected TIN models of

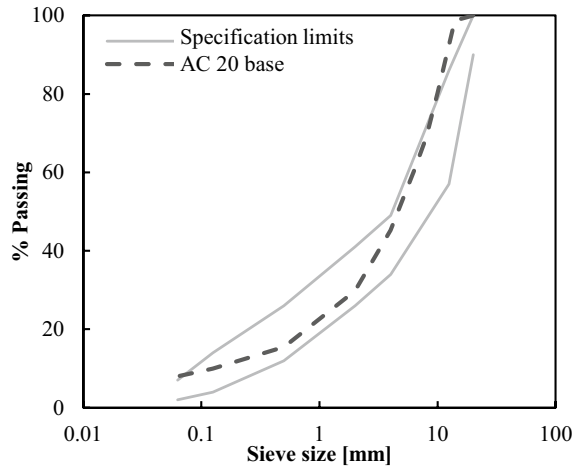

Fig. 4 Asphalt gradation curve–AC 20 base 40/60 [39]

individual aggregate particles were measured relative to the dimensions (long, D^L, intermediate, D^I, and short, D^S), the volume (V) and surface area (A). To measure the TIN model dimensions, it was implemented in MATLAB a numerical procedure using the Möller–Trumbore ray-triangle intersection algorithm [41, 42], which mimics the manual measurement method defined by Krumbein [43]. The measurement procedure is as follows:

- Long dimension (length) (D^L) is the distance between the two most distant peripherical points on the aggregate surface;
- Intermediate dimension (width) (D^I) is the longest distance between surface points in a direction perpendicular to the long axis;
- Short dimension (thickness) (D^S) is the longest distance between surface points in a direction perpendicular to the plane parallel to the long and intermediate axes.

It should be noted that the three-dimensional lines corresponding to D^L, D^I and D^S are perpendicular to each other but do not necessarily intersect at a single point.

Cubically shaped aggregates, with most or all surfaces created through crushing processes (i.e. broken surfaces), are desired to achieve high density particle packing and strong aggregate interlocking in bituminous mixtures. The three linear dimensions (D^L, D^I and D^S) are used to describe the shape or form

of a particle, and to identify particles with unwanted shapes (e.g., flat and elongated). However, as described in detail by Blott and Pye [44], the angularity or irregularity of a particle's surface is characterised by small indentations and depressions in the 3D representation of the particle, which is independent of the particle shape. In this study, however, the surface texture observed in the CT scan-derived 3D models was lost during the reconstruction process with the TIN model. Hence, the following shape indexes/ratios were considered:

Shape index (*SI*) (EN 933-4 [45]): measured with a calliper, the particle (4-63 mm sieve size) is considered non-cubical when $SI > 3$.

$$SI = \frac{D^L}{D^S} \tag{18}$$

Flatness ratio (*F*) [44]: classification system (0–0.2 extremely flat; 0.2–0.4 very flat; 0.4–0.6 moderately flat; 0.6–0.8 slightly flat; 0.8–1.0 not flat).

$$F = \frac{D^S}{D^I} \tag{19}$$

Flakiness index (*Fl*) (EN 933-3 [46]): measured with a specific grid/bar sieve, which detects the particles with a thickness less than half of the largest sieve fraction dimension (D^{max}), *i.e.* $Fl < 0.50$ (e.g., for the aggregate fraction 4/5 mm the distance between bars is 2.5 mm).

$$Fl = \frac{D^S}{D^{max}} \tag{20}$$

Elongation ratio (*E*) [44]: classification system (0–0.2 extremely elongate; 0.2–0.4 very elongate; 0.4–0.6 moderately elongate; 0.6–0.8 slightly elongate; 0.8–1.0 not elongate).

$$E = \frac{D^I}{D^L} \tag{21}$$

(true) Sphericity index (ψ^w) [47]: Wadell defined the degree of true sphericity as the ratio of the surface area of a sphere of the same volume as the particle (A^S), and the surface area of the particle (*A*). In this case, a sphere particle has an index of 1.0.

$$\psi^w = \frac{A^s}{A} \tag{22}$$

(working) Sphericity index (ψ^A) [48]: Aschenbrenner proposed, based on the tetrakaidekahedron solid, an expression to determine the degree of true sphericity from the three linear dimensions (D^L, D^I and D^S) of particles. In this case, a sphere particle ($D^L = D^I = D^S$) has an index of 0.96.

$$\psi^A = \frac{12.8\sqrt[3]{\left(D^S/D^I\right)^2\left(D^I/D^S\right)}}{1+\left(D^S/D^I\right)\left(1+\left(D^I/D^L\right)\right)+6\sqrt{1+\left(D^S/D^I\right)^2\left(1+\left(D^I/D^L\right)^2\right)}} \tag{23}$$

Table 1 lists the minimum, maximum and average values of the dimension and shape properties for the 82 selected aggregates. Most TIN models contain many points and facets to provide a detailed representation of particle geometry. Only nine models include fewer than 100 facets, which, according to [23], is the minimum threshold required to avoid compromising the accuracy of numerical simulations. The dimensions of these aggregates show a wide variation, ranging from 0.32 mm to 18.66 mm. As suggested by Qian et al. [19], the intermediate dimension is preferably used to define particle size, as it corresponds to the results obtained through an experimental sieve analysis procedure. Thus, the number of aggregates in different sieve fractions is as follows: 1 in 12.5/16 mm; 4 in 10/12.5 mm; 12 in 6.3/10 mm; 14 in 4/6.3 mm; 27 in 2/4 mm; 17 in 1/2 mm; 6 in 0.5/1 mm; and 1 in 0/0.5 mm. Notably, there was a

Table 1 Geometrical properties of digital aggregates

	Property	Min	Average	Max
TIN model	Points	25	167	411
	Facets	46	330	818
Dimension	Long, D^L [mm]	1.02	5.95	18.66
	Intermediate, D^I [mm]	0.48	3.94	12.59
	Short, D^S [mm]	0.32	2.56	8.83
	Volume, *V* [mm^3]	0.07	84.23	851.22
	Area, *A* [mm^2]	1.05	80.60	511.19
Shape ratio	Shape index, *SI* ($D^I \geq 4$ *mm*)	1.50	2.55	4.68
	Flatness, *F*	0.37	0.64	0.91
	Flakiness, *Fl* ($D^I \geq 4$ *mm*)	0.31	0.57	0.85
	Elongation, *E*	0.39	0.70	0.97
	(True) Sphericity, ψ^w	0.73	0.86	0.96
	(Working) Sphericity, ψ^A	0.68	0.85	0.94

clear sub-representation of both the largest coarse aggregate fractions (16/20 and 12.5/16) and the fine aggregates (<2 mm). This underrepresentation occurred for two primary reasons. First, in the 3D aggregate model derived from the CT scan, most of the largest aggregates had at least one face defined by the sawing process used to reduce the specimen size for scanning, leading therefore to their exclusion. Second, most fine aggregate particles were not considered for selection, as they are regarded as part of the bituminous mastic rather than directly represented in the DEM model. The bituminous mastic is a mixture of bitumen, filler and fine aggregate that covers the coarse aggregate particles and binds the aggregate skeleton. Thus, in previous studies [14, 49] the aggregates smaller than 2 mm were included in the mastic fraction of the DEM assembly.

Regarding particle shape, the average values of various indexes indicate that most particles had an acceptable shape for inclusion in bituminous mixtures. Following the European specifications for coarse aggregates [45, 46], of the 31 particles larger or equal to 4 mm, 11 were flake-shaped ($Fl < 0.50$) and 6 were non-cubical ($SI > 3$). In addition, following the classification for flat and elongated shapes proposed by Blott and Pye [44], 19 particles were moderately flat, 3 were very flat, 15 were moderately elongated, and 2 were very elongated. However, despite the presence of undesired particle shapes, the sphericity index values were generally high, with some particles approaching the shape of a perfect sphere.

Furthermore, given the large number of geometrical parameters involved, Table 2 presents the Pearson correlation matrix of the geometrical parameters to explore the possibility of reducing the number of variables required to describe particles in future studies. The three linear dimensions, volume, and surface area are strongly correlated (values >0.8), but only the short dimension (D^S) is reasonably correlated (values >0.6) with some shape indexes (*SI* and *Fl*). Among the shape indexes, as expected, the two sphericities are strongly correlated (0.89), and both are very correlated with other shape indexes, except for elongation. Therefore, elongation (*E*) showed a poor correlation with any other geometrical variable. Based on these findings, the three linear dimensions of particles are necessary for sieve classification, and at least one shape indicator, such as the shape index (*SI*) or the flatness index (*F*) should be determined.

To create DEM models with VirtualPM3DLab, these TIN models were used to establish the aggregate digital library in the DEM tool. The selected TIN models varied in size, and none were considered to have unwanted shapes (e.g., flat and elongated). As described in Sect. 3.2.2, to insert each aggregate, first, a TIN model is randomly chosen from the library, and then the circumscribed sphere radius of the model is adjusted to a random size within the minimum and maximum limits for the aggregate sieve fraction represented. Therefore, considering the current stage of development of the DEM tool, this digital library provides sufficient geometric variation for representing aggregates in bituminous specimens.

Table 2 Pearson correlation matrix of the geometrical parameters

	D^L	D^L	D^S	V	A	SI	F	Fl	E	ψ^w	ψ^A
Long, D^L	**1.00**										
Intermediate, D^I	0.96	**1.00**									
Short, D^S	0.92	0.91	**1.00**								
Volume, V	0.87	0.88	0.89	**1.00**							
Area, A	0.95	0.95	0.93	0.98	**1.00**						
Shape index, SI	−0.24	−0.28	−0.71	−0.35	−0.35	**1.00**					
Flatness, F	0.15	0.05	0.38	0.18	0.16	−0.83	**1.00**				
Flakiness, Fl	0.25	0.02	0.62	0.24	0.24	−0.79	0.97	**1.00**			
Elongation, E	−0.31	−0.07	−0.17	−0.11	−0.15	−0.16	−0.32	−0.39	**1.00**		
(True) Sphericity, ψ^w	−0.34	−0.25	−0.06	−0.14	−0.21	−0.89	0.55	0.75	0.51	**1.00**	
(Working) Sphericity, ψ^A	−0.07	−0.03	0.24	0.11	0.06	−0.98	0.76	0.86	0.33	0.89	**1.00**

4.2 Assessment of the adopted aggregate inner particle sub-discretisation

Figure 5 illustrates the result of filling two different TIN model shapes (aggregate model #1 and a subdivided icosahedron) with small spheres of varying sizes. To examine the multi-sphere filling algorithm, a convex polyhedron with 80 triangular faces, 120 edges, and 42 vertices (the pentakis icosidodecahedron or subdivided icosahedron), which approximates the shape of a sphere, was paired with one aggregate model obtained from the CT scan images of a bituminous specimen. The circumscribed sphere diameter of the subdivided icosahedron was set to the intermediate dimension of aggregate model #1, i.e. the radius of the circumscribed sphere (R_s^{circ}) was 6.295 mm for both TIN models. In the first four scenarios shown in Fig. 5a and b, the spheres in the assembly have a uniform size, and their radius (R_s) increases from 0.50 mm to 2.00 mm. The number of spheres (N_s) filling the volume, indicated next to each figure, increases drastically as the size of spheres decreases, from 9 to 634 with model #1, and from 24 to 1568 with the subdivided icosahedron. On the other hand, the exterior surface of the sphere assembly becomes closer to the TIN's model surface as the sphere size decreases. Nian et al. [13] demonstrated that a smooth exterior surface can be achieved by introducing many particles that overlap to a significant extent. Alternatively, a good representation of the TIN model shape with fewer particles can be achieved using spheres of variables sizes. For example, assemblies of spheres with radii between 0.50 mm and 1.50 mm had the same number of spheres as those composed of single-size spheres of 1.00 mm, see fifth scenario of Fig. 5a and b.

The computational time of DEM simulations increases with the number of particles, being therefore important to establish a compromise between the quality of the material's mesostructure representation and the required simulation time. Figure 6 depicts how various variables affect the results produced by the multi-sphere filling algorithm.

Figure 6a and b illustrate the effect of the sphere radius on the number of spheres required to fill the volume of seven different TIN models (six aggregates and the subdivided icosahedron), all with the same circumscribed radius. For uniform-size assemblies (Fig. 6a), the number of spheres increases as the sphere size decreases, resulting in a higher ratio of R_s^{circ}/R_s. Conversely, for variable-size assemblies (Fig. 6b), the number of spheres decreases as the ratio of the maximum to the minimum sphere radius (R_s^{max}/R_s^{min}) increases. However, the specific TIN model significantly influences the size of the sphere assembly. For example, when $R_s^{max}/R_s^{min} = 1.0$ (see Fig. 6b), the number of spheres ($R_s = 0.5$ mm) varies from 634 for model #1 to 2079 for model #2. Figure 6c shows the relationship between the number of particles and various shape ratios (F, E, ψ^w and ψ^A) for the seven TIN models. The results indicate that none of these

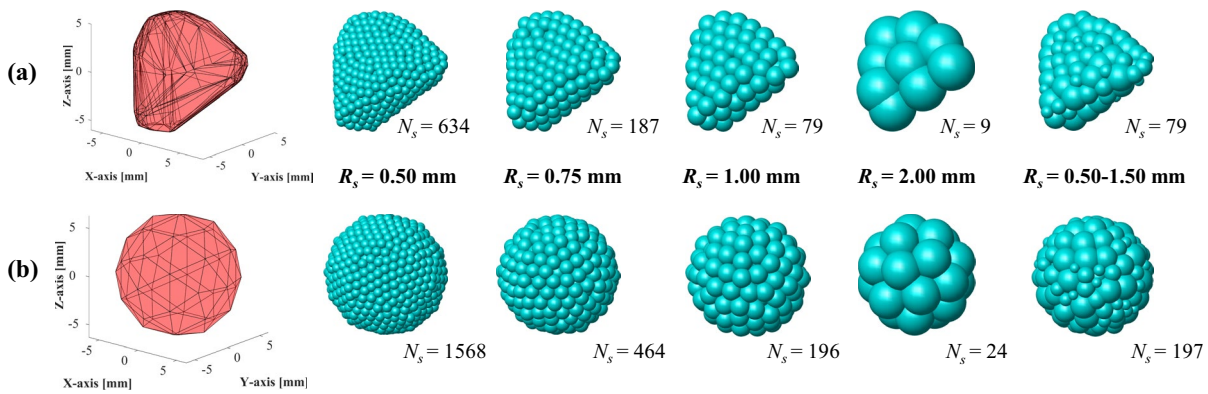

Fig. 5 Illustration of particles generated with the multi-sphere filling algorithm: **a** aggregate model #1; **b** icosahedron ($R_s^{circ} = 6.295$ mm)

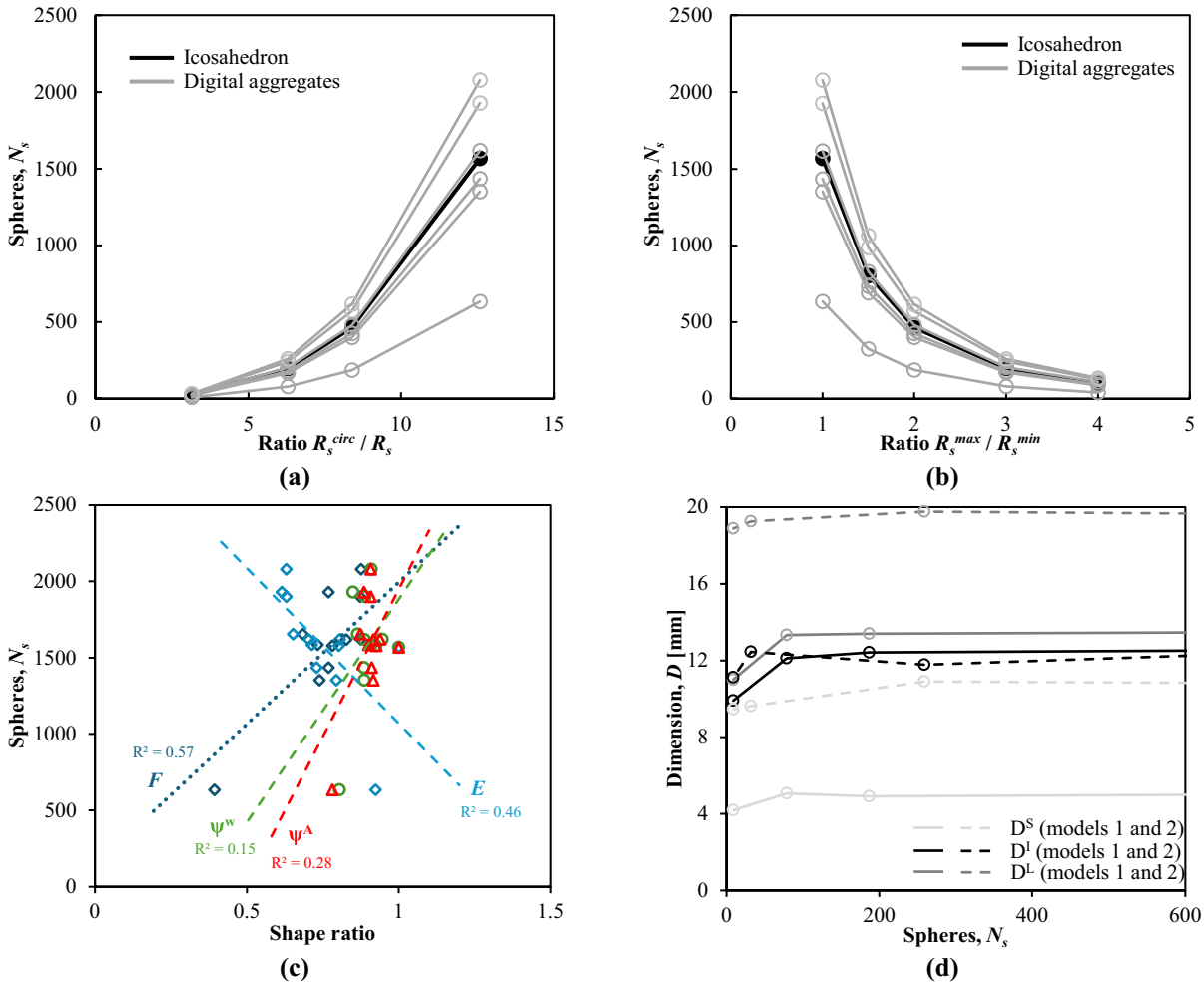

Fig. 6 Multi-sphere filling algorithm analysis: **a** N_s vs R_s^{circ}/R_s; **b** N_s vs R_s^{max}/R_s^{min}; **c** N_s vs shape ratio; **d** dimension (D^L, D^I and D^S) vs N_s

shape variables exhibit a strong correlation with the assembly size.

To determine the minimum number of particles required to effectively capture the shape and size of particles, Fig. 6d plots the three dimensions of two models as a function of the assembly size. The results indicate that the minimum assembly size, defined as the number of particles beyond which the dimensions remain nearly constant, varies depending on the TIN model. For example, the minimum size is 79 particles for aggregate model #1 (see Fig. 5a, $R_s = 1.00$ mm) and 259 particles for model #2. This corresponds to an intermediate level of discretisation quality, and a balance between computational efficiency and geometric accuracy.

4.3 Virtual asphalt specimen generation

The proposed asphalt representation that consider real aggregate particle shapes was tested within the DEM framework by modelling a conventional bituminous mixture for surface courses, AC 14 surf 35/50, which was designed and characterised in [50]. The weight proportions of different aggregate fractions are the following: 16.3% (12.5/19 mm); 12.5% (9.5/12.5 mm); 23.4% (4.75/9.5 mm);

15.3% (2.0/4.75 mm); 15.6% (0.425/2.0 mm); 7.5% (0.180/0.425 mm); 4.1% (0.075/0.180 mm); and 5.3% (<0.075 mm). The bitumen content by weight is 5.2%. Previously, Câmara et al. [14] modelled this bituminous mixture using the VirtualPM3DLab tool, where both the aggregate and mastic particles were represented as single spheres. The prismatic specimen with dimensions $50\times50\times80$ mm^3 was discretised into 35,760 spherical particles, consisting of 1596 particles representing the aggregate (2.00/19.5 mm) and 34,164 representing the mastic. The filler and aggregate finer than 2.0 mm were included as part of the bituminous mastic, which coats the coarse aggregates. Also, to reduce the computational size of the assembly, the mastic volume was discretised using spheres with a radius between 0.75 mm and 1.0 mm. This assembly is referred to in this paper as SS (single-sphere particle assembly). Figure 7a–c illustrate the particles representing the four aggregate fractions, while Fig. 7d shows the combined particles of the SS virtual specimen, including both aggregate and mastic constituents. To complement the visual inspection of the virtual specimen, Fig. 7e and f present two orthogonal vertical sections.

The proposed asphalt particle generation procedure was adopted to construct the virtual specimen of AC 14 surf 35/50 with realistic aggregate shapes larger than 2 mm. Two virtual specimens, MS-Poly-fine and MS-Poly-coarse, were built using this procedure, with different sphere sizes used for the aggregate's discretisation to allow assessing the effect of sphere size. In MS-Poly-fine, the inner sphere radii were defined between 0.75 mm and 1.00 mm, while in MS-Poly-coarse, the inner radii ranged between 1.00 mm and 2.00 mm. The finer discretization used sphere sizes similar to those adopted to represent mastic volume,

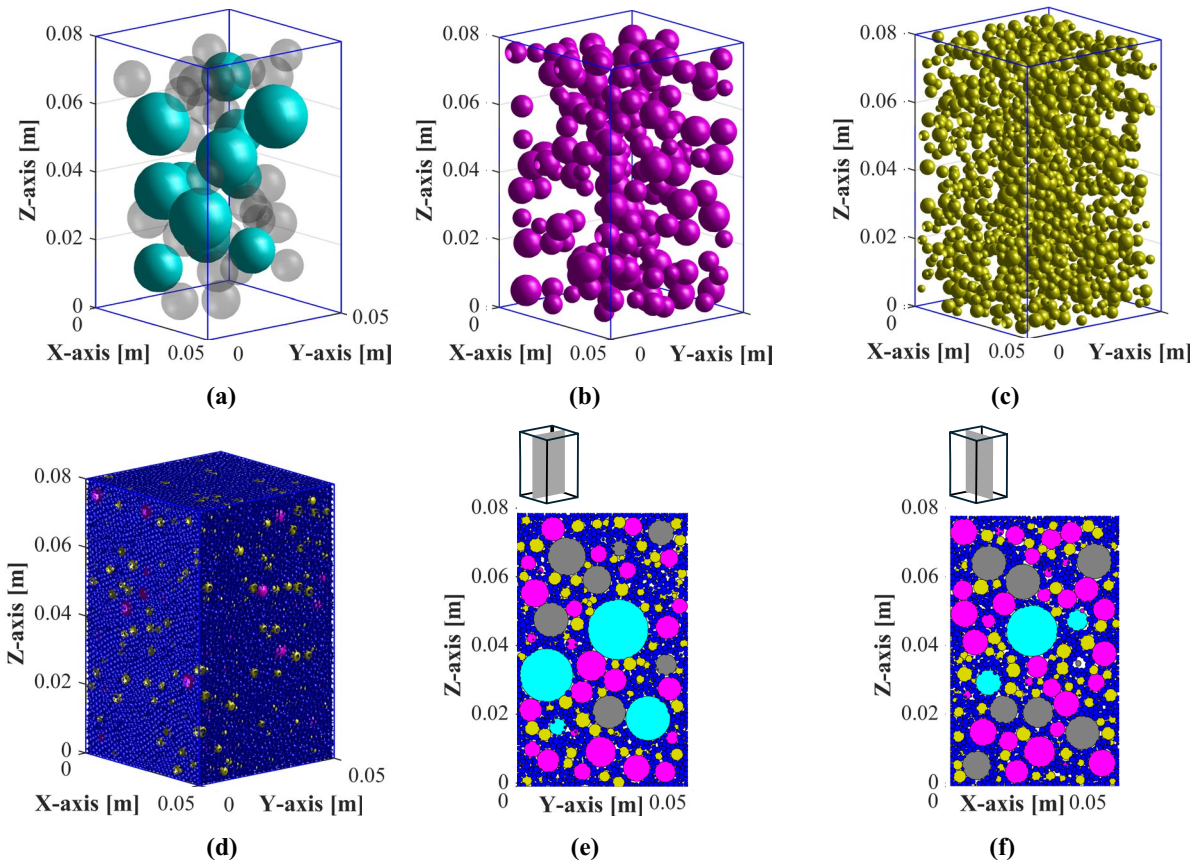

Fig. 7 Asphalt assembly w/ single-sphere particles (SS): **a** aggregate 9.5–19.0 mm (green 12.5–19.0 mm; grey 9.5–12.5 mm); **b** aggregate 4.75–9.5 mm; **c** aggregate 2.0–4.75 mm; **d** all particles (mastic—blue; other colours—aggregate); **e** 2D cross-section $x=0.025$ m; **f** 2D cross-section $y=0.025$ m

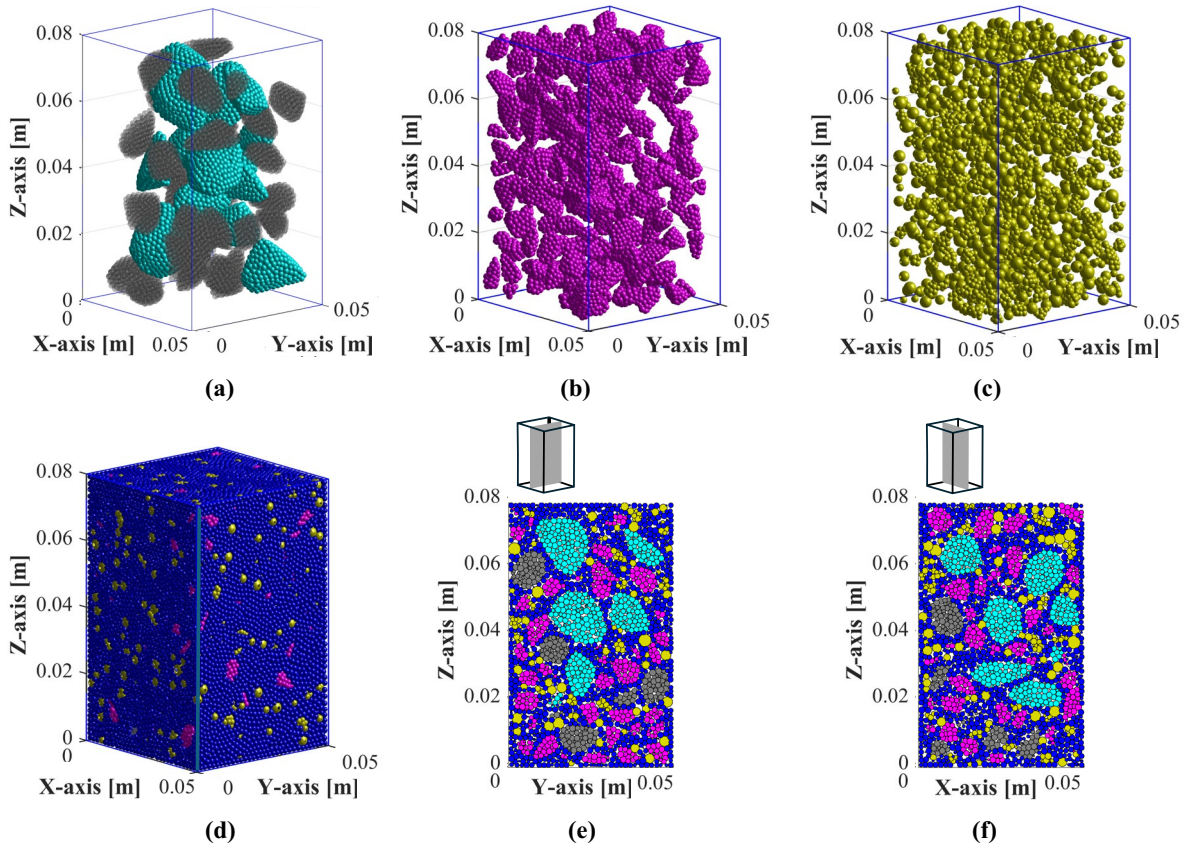

Fig. 8 Asphalt assembly w/ multi-sphere particles (MS-Poly-fine): **a** aggregate 9.5–19.0 mm (green 12.5–19.0 mm; grey 9.5–12.5 mm); **b** aggregate 4.75–9.5 mm; **c** aggregate 2.0–4.75 mm; **d** all particles (mastic—blue; other colours—aggregate); **e** 2D cross-section, $x = 0.025$ m; **f** 2D cross-section, $y = 0.025$ m

whereas the coarser discretization used sphere sizes between the maximum values of the finer discretization and the aggregate particles size considered to be part of the mastic. Figure 8a–c show the particles representing the four aggregate fractions, Fig. 8d shows all particles (aggregate and mastic), and Fig. 8e and f depict two orthogonal vertical sections of the MS-Poly-fine virtual specimen.

In addition, to enable a comprehensive analysis of the effect of the aggregate shape and deformability representation in DEM assemblies, two additional virtual specimens were built based on the TIN model of the subdivided icosahedron. The subdivided icosahedron is a convex polyhedron that approximates a spherical shape used in the conventional DEM assembly (SS). The new assemblies, MS-Ico-fine and MS-Ico-coarse, were generated using the same sphere size ranges defined for the aggregate's discretisation in MS-Poly-fine and MS-Poly-coarse, respectively.

Table 3 summarises the particle geometry of the aggregate and mastic fractions across the different DEM assemblies. The volume proportion and the average particle size within each fraction remained similar between the virtual specimens with single-sphere and multi-sphere aggregate representations. To ensure complete generation of particle assemblies within a reasonable computational time, a maximum number of insertion attempts was defined for randomly locating suitable regions in the specimen for aggregate placement. If the insertion procedure fails, additional rotations are applied to the aggregate particle and the insertion procedure is restarted. Due to the complexity of the aggregate shapes, predicting and resolving insertion challenges in advance is

Table 3 Composition of virtual asphalt assemblies

	Aggregates (min–max) [mm]				Mastic	Total
	12.5–19	9.5–12.5	4.75–9.5	2.0–4.75		
Design formulation						
Volume	14.0%	11.0%	20.7%	13.6%	40.7%	100.0%
Single-sphere particle assembly–SS						
Particles, N_p	12	27	184	1373	34,164	35,760
Spheres, N_s	12	27	184	1373	34,164	35,760
L^I (average)	15.6	10.8	6.8	3.1	1.7	
R_s (average)	7.8	5.4	3.4	1.6	0.9	
$\Sigma V_s/\Sigma V_s^{total}$	12.6%	9.1%	17.0%	13.2%	48.1%	100.0%
Multi-sphere particle assembly–MS-Poly-coarse						
Particles, N_p	12	32	225	1159	32,660	34,088
Spheres, N_s	1533	1198	1705	1159	32,660	38,255
L^I (average)	14.8	10.2	6.9	3.3	1.7	
R_s (average)	1.5	1.5	1.6	1.7	0.8	
$\Sigma V_s/\Sigma V_s^{total}$	11.4%	8.5%	16.0%	13.7%	50.4%	100.0%
Multi-sphere particle assembly–MS-Poly-fine						
Particles, N_p	14	31	264	1298	32,809	34,416
Spheres, N_s	7944	6283	11,737	4177	32,809	62,950
L^I (average)	15.0	10.5	6.2	3.8	1.7	
R_s (average)	0.9	0.9	0.9	1.1	0.8	
$\Sigma V_s/\Sigma V_s^{total}$	12.2%	9.4%	17.1%	12.3%	48.9%	100.0%
Multi-sphere particle assembly–MS-Ico-coarse						
Particles, N_p	14	33	264	1352	31,159	32,822
Spheres, N_s	1662	1250	1624	1352	31,159	37,047
L^I (average)	15.5	10.8	7.1	3.2	1.7	
R_s (average)	1.5	1.5	1.6	1.6	0.8	
$\Sigma V_s/\Sigma V_s^{total}$	11.9%	8.8%	16.5%	13.9%	48.8%	100.0%
Multi-sphere particle assembly–MS-Ico-fine						
Particles, N_p	16	30	258	1434	31,790	33,528
Spheres, N_s	8546	6620	12,387	4357	31,790	63,700
L^I (average)	14.9	11.2	6.5	3.9	1.7	
R_s (average)	0.9	0.9	0.9	1.0	0.8	
$\Sigma V_s/\Sigma V_s^{total}$	12.6%	9.6%	17.6%	12.4%	47.7%	100.0%

considerably more difficult than with a purely spherical insertion algorithm.

The total number of aggregate particles varied (decrease) by only 4–8% in the assemblies with sub-discretised aggregate particles. However, the number of spheres increased by 4–7% with larger spheres ($R_s = 1.00$–2.00 mm) and by 76–78% with smaller spheres ($R_s = 0.75$–1.00 mm). Evidently, a significant larger number of spheres are necessary to fill the TIN model of the aggregate being represented when smaller spheres are admitted for the inner particle discretisation.

In the MS assemblies, the number of spheres per particle varied from 1 to 892. The implemented multi-sphere filling algorithm enforces a minimum of eight spheres to represent the aggregate. Otherwise, the aggregate is represented by a single sphere with a radius equal to the circumscribed radius of the TIN model. In the cases of MS-Poly-coarse and MS-Ico-coarse, all aggregates within the 2.0–4.75 mm size range were represented by a single sphere. Additionally, the composition of the MS assemblies was similar for the same size range of spheres, regardless of whether the aggregates were modelled using realistic shapes from the digital library and the regular subdivided icosahedron shape.

The mesostructure of real bituminous specimens is defined by the distribution, segregation, and shape properties of its three phases (aggregate, bitumen and air voids) within the bulk volume. These properties are influenced by factors, such as aggregate gradation, particle shape, bitumen content, and compaction. For instance, Hunter et al. [51] analysed aggregate particle orientation in horizontal cross-sections of bituminous specimens compacted using different methods and observed a circumferential alignment of aggregate particles in specimens compacted with the gyratory and vibratory compactors.

Thus, the aggregate particle orientation is one variable that can be used to evaluate the mesostructure of both real and virtual bituminous specimens. In virtual assemblies, the particle orientation is significant in multi-sphere (MS) assemblies, as opposed to single-sphere representations where particle orientation is irrelevant due to the absence of a preferred direction. Figure 9a and b show the maximum dimension line of aggregate particles larger than 4.75 mm in the MS-Poly-fine and MS-Poly-coarse assemblies, respectively. In the MS-Poly-coarse assembly, smaller aggregate particles in the 2.0–4.75 mm size range are represented as single spheres, and hence their directions are not shown. Also, Fig. 9a shows more direction lines than Fig. 9b due to the higher number of multi-sphere particles in MS-Poly-fine. Overall, the maximum dimension lines of aggregate particles are well distributed across the specimen volume, showing no clear preferred orientation. This is further validated in Fig. 9c, where the cumulative distribution lines of the individual vector components (X, Y and Z) for the maximum dimension lines in Fig. 9a and b are plotted. The results demonstrate an almost equal distribution of vector components in all directions, confirming that the implemented algorithm distributes well the aggregate particles throughout the virtual specimen volume.

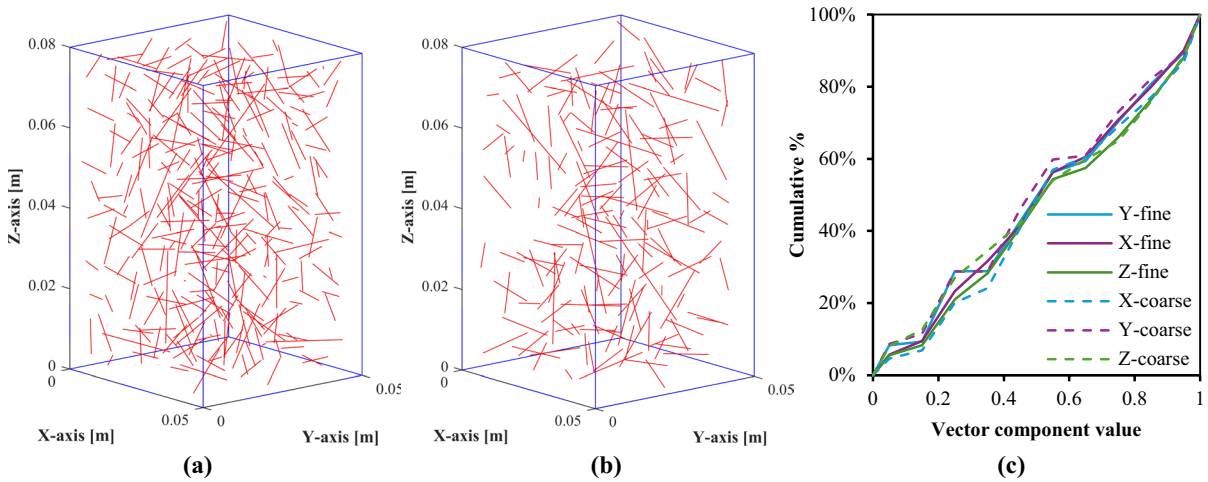

Fig. 9 Multi-sphere particles orientation: **a** D^L line (MS-Poly-fine); **b** $D.^L$ line (MS-Poly-coarse); **c** cumulative frequency of vector component values (x-, y- and z-axes)

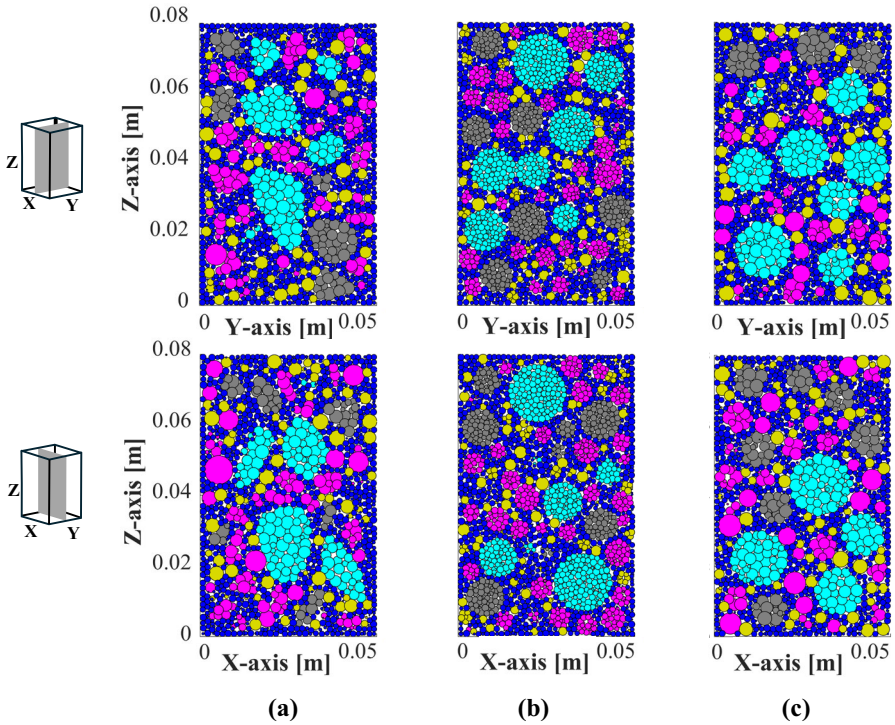

Fig. 10 2D cross-sections of asphalt assemblies (top, $x = 0.025$ m; bottom, $y = 0.025$ m): **a** MS-Poly-coarse; **b** MS-Ico-fine; **c** MS-Ico-coarse

In summary, to illustrate the mesostructure of the assemblies not previously shown, Fig. 10 presents two orthogonal vertical sections of the MS-Poly-coarse, MS-Ico-fine and MS-Ico-coarse assemblies. As referred before, the aggregate skeleton of compacted bituminous mixtures plays a crucial role in load dispersion within the material, directly impacting its stiffness properties.

4.4 Effect of deformable multi-sphere aggregate particles on asphalt viscoelastic stiffness properties

The viscoelastic stiffness properties of the bituminous mixture AC 14 surf 35/50, along with several variations of its reference formulation, were characterised by means of an uniaxial cyclic testing protocol as detailed in [50]. The test consisted of applying a cyclic tension–compression load with a vertical strain amplitude of 1×10^{-4} m/m, across multiple frequencies, to prismatic specimens with dimensions $50 \times 50 \times 80$ mm^3, conditioned at a temperature of 20 ºC. Câmara et al.[14] reproduced these experiments numerically with the DEM tool VirtualPM3DLab. The simulated particle assembly (SS, single-sphere particle assembly) was loaded through a vertical displacement imposed on the top wall. The top wall was constrained in the horizontal directions, while the bottom wall was fully fixed. At each loading frequency, the complex stiffness modulus ($|E^*|$) and phase angle (ϕ) were calculated from the applied strain and the stress response:

$$|E^*| = \frac{\sigma_{max} - \sigma_{min}}{\varepsilon_{max} - \varepsilon_{min}} \tag{24}$$

$$\phi = 360 \frac{\Delta t}{T} \tag{25}$$

where, σ_{max} and σ_{min} are the maximum and minimum stress in a cycle, ε_{max} and ε_{min} are the corresponding strains, T is the loading period, and Δt is the time lag between the stress and strain peaks.

To improve agreement between simulations and experiments, Câmara et al.[14] adjusted the DEM model contact configuration. The best

correspondence was achieved by assigning a generalised Kelvin viscoelastic contact model to mastic-mastic (*M-M*) and mastic-aggregate (*M-A*) contacts, while aggregate-aggregate (*A-A*) and aggregate/mastic-to-loading plate (*A/M-W*) contacts were treated as linear elastic. The initial *M-M* contact parameters were obtained by fitting the generalised Kelvin model to the experimentally measured viscoelastic properties of the mastic. The modulus for the *A-A* contact (linear elastic model) was estimated by admitting 2 springs in series, based on the material properties reported by [50] (Elastic modulus: 60 GPa; Poisson coefficient: 0.28). The calibration factor δ values were determined through a trial-and-error fitting procedure to approximate the experimental response under the uniaxial cyclic testing protocol. First, the response of the mastic specimen was simulated to determine the δ value for *M-M* contacts. Afterwards, the bituminous mixture was simulated to determine the δ value for *M-A* contacts, assuming that the corresponding viscoelastic response results from the linear elastic model for *A-A* contacts in series with the viscoelastic model for *M-M* contacts. The δ value for *M-M* contacts was assumed to remain the same in both mastic and bituminous specimens.

Table 4 summarizes the contact properties for the reference material (AM1) and for the variant with an alternative bitumen (AM2) in the normal direction. The calibrated values of the ratio coefficient α were 0.10 for *M-M*/*M-A* contacts, 0.05 for *A-A* and 0 for *A-W*. The calibrated δ values were: 1.88 (*M-M*), 3.15 (*M-A*) and 1.00 (*A-A*) for AM1; 1.90 (*M-M*), 6.75 (*M-A*) and 1.00 (*A-A*) for AM2.

In this study, the internal aggregate contacts of multi-sphere particles were calibrated by simulating a cubic aggregate ($20\times20\times20$ mm^3) subjected to uniaxial compressive loading. For this purpose, two cubic aggregates were built using different sizes of spheres ($R_s = 0.75$–1.00 mm and 1.00–2.00 mm), which correspond to the sphere sizes used in the "fine" and "coarse" MS assemblies. The contact moduli determined for these configurations were 1.125×10^8 kPa and 1.116×10^8 kPa, with $\alpha = 0.05$ for the "fine" and "coarse" discretisation of aggregate particles, respectively. The density of aggregate particles (granite) is 2.63 g/cm^3 and of mastic is 2.11 g/cm^3.

The viscoelastic stiffness modulus and phase angle values at various loading frequencies (2, 5, 10 and 20 Hz) for the SS and MS assemblies representing the AM1 mixture are shown in Fig. 11. Experimental data are not shown, as the objective of this study was to evaluate the influence of modelling coarse aggregates as deformable clusters of spherical particles on the volumetric properties and on the mechanical response of DEM assemblies. The obtained results with the deformable aggregates are compared with the calibrated single-sphere (SS) assembly [14]. Thus, to compare the effect of the assembly on $|E^*|$ and ϕ values, Fig. 11 also shows the relative deviation (d_m) values, which are determined as:

$$d_m = \frac{X - X_{ref}}{X_{ref}} \tag{26}$$

Table 4 Contact properties (normal direction) [14]

Contact type	Material	E_m	E_1	E_2	E_3	C_m	C_1	C_2	C_3
M-M	AM1	1.115×10^7	3.799×10^5	1.600×10^6	4.308×10^7	2.515×10^6	8.950×10^6	5.695×10^6	1.114×10^6
	AM2	8.909×10^6	1.064×10^7	6.326×10^6	5.776×10^7	1.164×10^6	2.854×10^5	5.865×10^5	5.354×10^6
M-A	AM1	3.511×10^7	1.197×10^6	5.039×10^6	1.357×10^8	7.921×10^6	2.819×10^7	1.794×10^7	3.510×10^6
	AM2	6.014×10^7	7.184×10^7	4.270×10^7	3.899×10^8	7.859×10^6	1.925×10^6	3.959×10^6	3.614×10^7
A-A/*A-W*	AM1/AM2	1.151×10^8							
M-W	AM1	3.511×10^7							
	AM2	8.909×10^6							

Units: *E* (kPa); *C* (kPa.s)

The contact properties adopted for each contact type already take into account the corresponding calibration coefficient

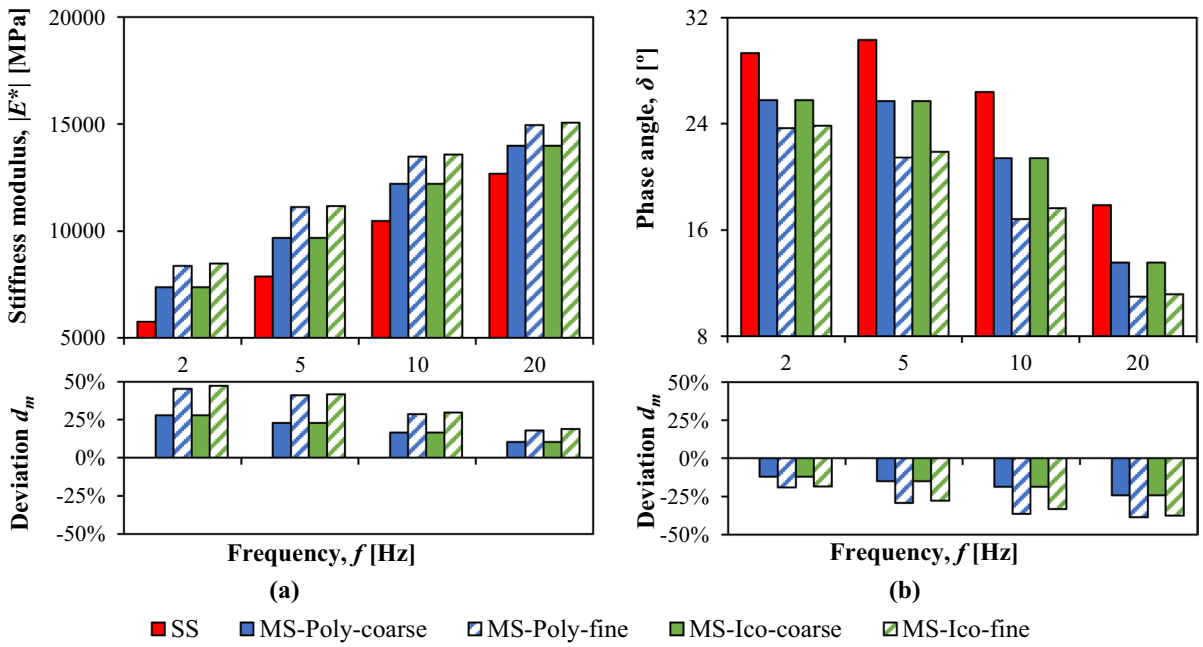

Fig. 11 Variation of viscoelastic stiffness properties with frequency of different assemblies (constant δ values) for AM1 mixture: **a** stiffness modulus; **b** phase angle

where, X and X_{ref} are the values for the assembly being analysed and the reference assembly. Herein, the reference assembly is SS.

Figure 11 shows that all assemblies exhibited the expected frequency-dependent behaviour, where the $|E^*|$ value increased and the ϕ value reduced, indicating a more elastic response to loading at higher frequencies. However, MS-assemblies exhibited higher $|E^*|$ values and lower ϕ values compared to SS, despite having similar aggregate and mastic proportions. Specifically, MS-poly-coarse and MS-Ico-coarse showed, compared to SS, an average increase of 19% in the stiffness modulus and a 18% decrease in the phase angle. In addition, MS-poly-fine and MS-Ico-fine showed average increases of 33% and 34% in stiffness modulus, and reductions of 31% and 29% in phase angle, respectively. Although the average deviations of each MS assembly were similar for the stiffness modulus and the phase angle, the deviation of each variable was affected by the loading frequency. For the stiffness modulus, the deviation increased with frequency, while the opposite trend was observed for the phase angle.

These results demonstrate that introducing deformable clusters of spherical particles to represent coarse aggregates has a pronounced effect on the response of 3D DEM assemblies. Because the subdivided icosahedrons in the "MS-Ico" assemblies approximate the spherical particle geometry used in the conventional DEM assembly (SS), it can be concluded that these deformable particle clusters introduce a stiffening and more elastic response in the DEM models. Conversely, when comparing the "MS-Poly" and "MS-Ico" assemblies to assess the influence of aggregate particle shapes, only small variations were observed in the $|E^*|/\phi$ values. For assemblies with a coarse internal discretisation of the aggregates, these values were essentially identical, and for those with a finer internal discretisation, differences of only 0.8% in $|E^*|$ and 2.3% in ϕ were observed (with higher values for the "Ico" assembly). These findings suggest that the observed effects are primarily governed by the

internal discretisation of the coarse aggregates and the interactions among mixture constituents within the assembly.

Table 5 lists the number of contacts per type in the assemblies. All contacts between spheres belonging to different aggregates were counted, excluding internal contacts within multi-sphere particles. Overall, MS assemblies with a coarser internal discretisation of aggregates exhibited only a slightly higher (1–5%) total number of contacts than the SS assembly, while those with a finer internal discretisation showed a larger variation (27–32%). The coordination number also reflects the variation on the contact network among assemblies.

However, when comparing the number of contacts by type in MS assemblies to those in SS, the number of *A-A* contacts increased by 84%, 78%, 355% and 304% for MS-poly-coarse, MS-Ico-coarse, MS-poly-fine, MS-Ico-fine, respectively. For *M-A* contacts, the increases were 33%, 34%, 136% and 127%, respectively, while *M-M* contacts decreased only slightly (6%-13%). Consequently, the higher number of aggregate interactions, particularly in MS-poly-fine and MS-Ico-fine assemblies, resulted in a stiffer and more elastic numerical response. The effect on stiffness modulus was more pronounced at the lowest simulated loading frequency, where the mastic is softer due to its viscoelastic nature.

Table 5 Particle-to-particle contacts of virtual asphalt assemblies

	Contacts (excluding inner contacts)				Coordination number
	A-A	*M-A*	*M-M*	Total	
SS	2177	55,451	154,222	211,851	5.92
MS-Poly-coarse	4014	73,731	144,390	222,135	6.52
MS-Poly-fine	9902	130,989	138,699	279,592	8.12
MS-Ico-coarse	3875	74,180	135,092	213,147	6.49
MS-Ico-fine	8788	126,088	134,849	269,728	8.04

A Aggregate, *M* Mastic

The deformation response to loading in dense- and gap-graded bituminous mixtures under loading is highly influenced by aggregate-aggregate load transmission and the locking structure formed during compaction. Previous studies suggest that cubical-shaped particles provide better interlock than spherical ones [1]. However, the present results show that the DEM assemblies were more sensitive to the sphere size used for the aggregate-volume discretisation than to the aggregate shape itself. Whether using irregular particle models from the library ("Poly" assemblies) or subdivided icosahedron models ("Ico" assemblies), aggregate shape had only a minimal effect on the total number of contacts, the distribution of contacts among different constituents, and, consequently, on the viscoelastic stiffness properties. These findings highlight the significant influence that the chosen aggregate-representation method can have in DEM modelling.

To approximate the DEM response with different assemblies, new calibration factors for *M-A* contacts in the multi-sphere assemblies were determined, yielding $|E^*|$ values similar to those of the single-sphere assembly SS. All assemblies have similar mastic and aggregate proportions (see Table 3). The δ factor for *M-M* contacts remained unchanged, as the mastic was represented with single spheres of the same size range in all assemblies (SS and MS). Figure 12 shows the $|E^*|$ and ϕ values, along with the relative deviations from SS for the calibrated assemblies. The δ factor values were 1.68 for MS-Poly-coarse and MS-Ico-coarse, and 1.00 for MS-Poly-fine and MS-Ico-fine, compared with initial value of 3.15. With these calibration factors, the average d_m for $|E^*|$ was only 3% for the four assemblies. However, the d_m values for ϕ variable varied between -16% to $+15\%$, demonstrating the challenge of controlling this variable in DEM simulations.

To validate the ability to reduce the calibration factors values with the developed approach, DEM simulations for the AM2 mixture in [14] were repeated

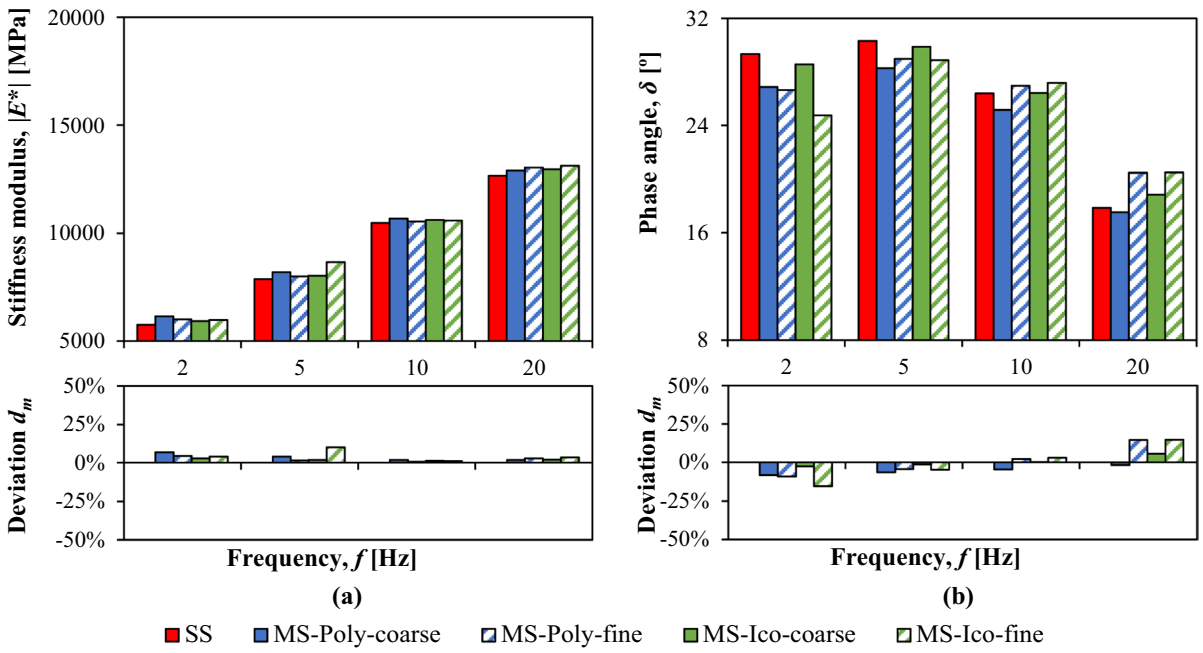

Fig. 12 Variation of viscoelastic stiffness properties with frequency of different assemblies (individual calibration, δ values) for AM1 mixture: **a** stiffness modulus; **b** phase angle

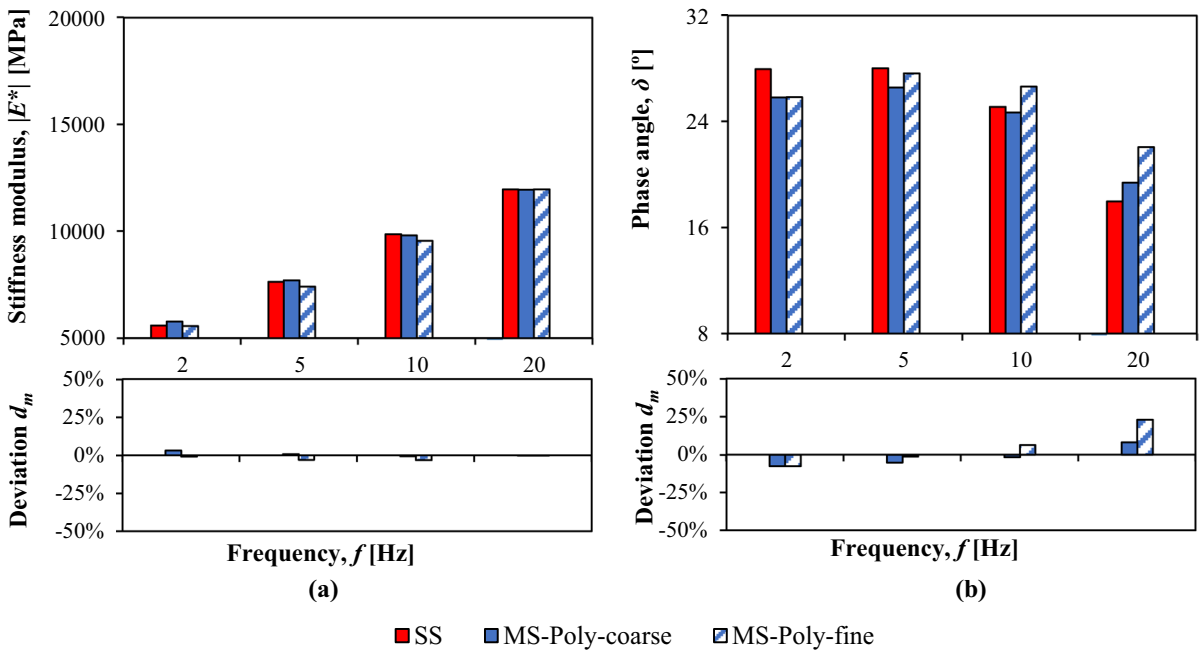

Fig. 13 Variation of viscoelastic stiffness properties with frequency of different assemblies (individual calibration, δ values) for AM2 mixture: **a** stiffness modulus; **b** phase angle

using these assemblies, with new calibration factors determined. Figure 13 shows the $|E^*|$ and ϕ values for the calibrated assemblies and the relative deviation from SS. The d_m values ranged from -3% to $+3\%$

for $|E^*|$, and from -8% to $+23\%$ for ϕ. The δ factor values for *M-A* contacts were 6.75 for SS, 3.20 for MS-Poly-coarse, and 1.70 for MS-Poly-fine.

In conclusion, the numerical simulation of the viscoelastic loading response of bituminous mixtures was significantly improved by discretising coarse aggregates with small spherical particles. This improvement was especially noticeable in terms of the stiffness modulus. The phase angle, however, exhibited larger variations, indicating the need for further investigation of the influence of DEM model parameters.

Aggregate shape had only a small influence on the number of contacts between the different bituminous mixture constituents and, consequently, on the viscoelastic stiffness properties ($|E^*|$ and ϕ). The greater sensitivity of the DEM models to the number of *A–A* and *M–A* contacts, rather than to aggregate shape, is likely related to the use of Laguerre–Voronoi diagrams in VirtualPM3DLab, which even for the SS model approximate spherical particles with polyhedral Voronoi shapes. These diagrams define spherical particle contacts and contact areas in a way that effectively maps the domain of spherical particles onto that of polyhedral aggregate shapes, thereby diminishing the direct influence of detailed aggregate geometry on the mechanical response. Future studies will further investigate this effect by modelling bituminous specimens with variable compositions and under different loading conditions.

Long computation times are a well-known limitation of 3D DEM simulations, as they generally increase with the number of particles and contacts. In this study, the simulations were performed on a desktop computer equipped with an Intel i9-10900KF @ 3.70 GHz multi-core processor. The shortest computation times were obtained for the rigid aggregate assembly SS, ranging from 3 days at 20 Hz to 16 days at 2 Hz. In contrast, the longest times were recorded for the assembly MS-Poly-fine, ranging from 5 days at 20 Hz to 40 days at 2 Hz. The MS assemblies with coarser aggregate discretisation (MS-Poly-coarse and MS-Ico-coarse) exhibited computation times similar to SS, varying from 3 days at 20 Hz to 17 days at 2 Hz. To improve efficiency, future developments of VirtualPM3DLab will focus on implementing parallel processing techniques, as suggested by Skorych and Dosta [52].

5 Conclusions

This paper presented and evaluated a methodology for incorporating complex aggregate shapes into DEM models of bituminous mixtures. The proposed methodology involved constructing a digital library of aggregate shapes obtained from X-ray computed tomography scans of a single bituminous specimen and modelling these shapes in the numerical assembly using clusters of small spherical particles. This method enables a realistic representation of the complex geometry of coarse aggregates and accounts for their deformability, which arises from the contacts between the inner particles. These developments were implemented in VirtualPM3DLab, an advanced 3D DEM software program that employs Laguerre–Voronoi diagrams to define spherical particle contacts and contact areas, and a generalised Kelvin contact model to represent the viscoelastic behaviour of bituminous materials. The main conclusions drawn from this study are as follows:

- A large number of triangulated surface models of individual aggregates can be directly obtained by applying the CT image processing procedure to a single small-sized bituminous specimen. The resulting surface models had geometrical properties consistent with those expected for the specific bituminous mixture scanned. However, the surface detail of the aggregate model can be reduced if computational resources are limited during DEM simulations. Additionally, the digital library of aggregate shapes should include enough models to represent the variety of particles in aggregates of different mineralogical origins and size fractions. It does not need to be extremely large if algorithms are implemented to generate more models from seed models (e.g., resizing a seed model to use the shape in a different size fraction).
- Discretising the aggregate surface model using a distribution of smaller-radius spherical particles effectively captures aggregate geometry while enabling particle deformability, which is particularly relevant for fracture studies. The adopted contact model also eliminates the need for the complex and computationally expensive contact-detection procedures required for polyhedral particles. However, the size distribution of the spheres

influences the resulting geometric properties and should therefore be carefully selected to improve the fidelity of the aggregate representation.

- The generation method, which fills the DEM specimen volume from the largest to the smallest aggregates, followed by the mastic, ensured an even distribution of multi-sphere aggregate particles without introducing preferred orientations. This approach allows for a coarser mastic assembly, improving computational efficiency, while enhancing the representation of aggregate surfaces through inner discretisation and Voronoi-based shapes.
- Representing aggregate particles as deformable bodies in the DEM model significantly influenced the simulated viscoelastic stiffness properties. Virtual asphalt specimens with multi-sphere aggregate particles exhibited higher stiffness moduli and lower phase angle values at various loading frequencies compared to single-sphere particle specimen. The variation in viscoelastic stiffness properties was greater with finer aggregate shape discretisation (i.e. smaller internal spheres), due to the significant increase in the number of aggregate-aggregate and aggregate-mastic contacts. However, finer discretisation also results in substantially higher computational costs.
- Contrary to the initial expectations, the aggregate shape had a minimal impact on the DEM simulations. In our view, this is because the total number of contacts, the distribution of contacts among different constituents were very similar for assemblies with irregular particle models from the library ("Poly" assemblies) or subdivided icosahedron models ("Ico" assemblies).
- The virtual specimens with multi-sphere aggregate particles required lower calibration coefficients between the mesoscopic and macroscopic properties. The δ value for the aggregate-mastic contact decreased in AM1 from 3.15 to 1.68 and 1.00, and in AM2 from 6.75 to 3.20 and 1.70, depending on the aggregate discretisation. These reductions suggest that the calibration factor in the conventional single-sphere aggregate model partly compensates for the aggregates being approximated as rigid bodies.

Nevertheless, the conclusions obtained relative to the effect of aggregate shape and deformability are based solely on the viscoelastic properties ($|E^*|$ and ϕ) determined under small deformations, representing the undamaged condition. Further work is underway to assess the effect of representing realistic aggregate shapes and deformability on the fracture properties of 3D DEM asphalt models, under uniaxial tensile and compressive loads, and at different temperatures.

Funding Open access funding provided by FCT|FCCN (b-on). This research was funded in whole or in part by the Fundação para a Ciência e a Tecnologia, I.P. (FCT,https://ror.org/00snfqn58) through the R&D unit: Civil Engineering Research and Innovation for Sustainability (CERIS) – UID/6438/2025. For the purpose of Open Access, the authors have applied a CC-BY public copyright license to any Author 's Accepted Manuscript (AAM) version arising from this submission.

Data availability The data that support the findings of this study are available from the corresponding author, [R.M], upon reasonable request.

Declarations

Conflict of interest The authors declare that they have no known competing financial interests or personal relationships that could have appeared to influence the work reported in this paper.

References

1. Hunter RN, Shelf A, Read J (2015) The Shell bitumen handbook, 6th ed. ICE Publishing, London
2. Vandewalle D, Antunes V, Neves J, Freire AC (2020) Assessment of eco-friendly pavement construction and maintenance using multi-recycled RAP mixtures. Recycling 5:17. https://doi.org/10.3390/recycling5030017
3. CEN (2016) EN 13108-1:2016 bituminous mixtures. Materials specifications. Part 1: asphalt concrete. European Committee for Standardization, Brussels

4. Yao H, Xu M, Liu J, Liu Y, Ji J, You Z (2022) Literature review on the discrete element method in asphalt mixtures. Front Mater. https://doi.org/10.3389/fmats.2022.879245
5. Ballhause D, König M, Kröplin B (2008) Modelling fabric-reinforced membranes with the discrete element method. In: Oñate E, Kröplin B (eds) Textile composites and inflatable structures II. Springer Netherlands, Dordrecht, pp 51–67. https://doi.org/10.1007/978-1-4020-6856-0_4
6. Feng R, Zhu B, Hu C, Wang X (2019) Simulation of nonlinear behavior of beam structures based on discrete element method. Int J Steel Struct 19:1560–1569. https://doi.org/10.1007/s13296-019-00228-0
7. Kaschube J, Dinkler D (2021) A discrete element model for reinforced concrete. PAMM 20:e202000258. https://doi.org/10.1002/pamm.202000258
8. Lu DX, Bui HH, Saleh M (2024) Predicting the rutting behaviour of asphalt concrete in the modified wheel tracking test using DEM and a cohesive viscoelastic–elastoplastic-damage contact model. Comput Part Mech. https://doi.org/10.1007/s40571-024-00756-5
9. You Z (2003) Development of a micromechanical modeling approach to predict asphalt mixture stiffness using the discrete element method. PhD thesis, University of Illinois at Urbana-Champaign
10. Lira B, Jelagin D, Birgisson B (2013) Gradation-based framework for asphalt mixture. Mater Struct 46:1401–1414. https://doi.org/10.1617/s11527-012-9982-3
11. Liu Y, You Z (2011) Accelerated discrete-element modeling of asphalt-based materials with the frequency-temperature superposition principle. J Eng Mech 137:355–365. https://doi.org/10.1061/(ASCE)EM.1943-7889.0000234
12. Liu W, Gao Y, Huang X, Li L (2018) Investigation of motion of coarse aggregates in asphalt mixture based on virtual simulation of compaction test. Int J Pavement Eng 0:1–13. https://doi.org/10.1080/10298436.2018.1447109
13. Nian T, Ge J, Li P, Guo R, Li J, Wang M (2022) Improved three-dimensional discrete modeling method and anti-cracking properties of asphalt mixture. Constr Build Mater 321:126405. https://doi.org/10.1016/j.conbuildmat.2022.126405
14. Câmara G, Azevedo NM, Micaelo R, Silva H (2023) Generalised Kelvin contact models for DEM modelling of asphalt mixtures. Int J Pavement Eng 24:2179625. https://doi.org/10.1080/10298436.2023.2179625
15. Peng Y, Gao H, Lu X, Sun L (2020) Micromechanical discrete element modeling of asphalt mixture shear fatigue performance. J Mater Civ Eng 32:04020183. https://doi.org/10.1061/(ASCE)MT.1943-5533.0003246
16. Liu Y, Zhou X, You Z, Yao S, Gong F, Wang H (2017) Discrete element modeling of realistic particle shapes in stone-based mixtures through MATLAB-based imaging process. Constr Build Mater 143:169–178. https://doi.org/10.1016/j.conbuildmat.2017.03.037
17. Valera RLR, González JI, de Oliveira Junior M, de Farias MM, Fuentes MAC, Martínez RT, Aguila JP, Anselmi LAM, Morfa CAR, Oñate E (2022) Development and coupling of numerical techniques for modeling micromechanical discrete and continuous media using real particle morphologies. Comp Part Mech. https://doi.org/10.1007/s40571-022-00481-x
18. Mollon G, Zhao J (2013) Generating realistic 3D sand particles using Fourier descriptors. Granul Matter 15:95–108. https://doi.org/10.1007/s10035-012-0380-x
19. Qian Z, Garboczi EJ, Ye G, Schlangen E (2016) Anm: a geometrical model for the composite structure of mortar and concrete using real-shape particles. Mater Struct 49:149–158. https://doi.org/10.1617/s11527-014-0482-5
20. Recarey C, Pérez I, Roselló R, Muniz M, Hernández E, Giraldo R, Oñate E (2019) Advances in particle packing algorithms for generating the medium in the discrete element method. Comput Methods Appl Mech Eng 345:336–362. https://doi.org/10.1016/j.cma.2018.11.011
21. Ma T, Zhang D, Zhang Y, Wang S, Huang X (2018) Simulation of wheel tracking test for asphalt mixture using discrete element modelling. Road Mater Pavement Des 19:367–384. https://doi.org/10.1080/14680629.2016.1261725
22. Garcia-Hernandez A, Wan L, Dopazo-Hilario S, Chiarelli A, Dawson A (2021) Generation of virtual asphalt concrete in a physics engine. Constr Build Mater 286:122972. https://doi.org/10.1016/j.conbuildmat.2021.122972
23. Wei X, Sun Y, Gong H, Chen J (2024) Determining appropriate level of detail of 3D aggregate model for accurate and efficient mesoscopic simulation of asphalt concrete. Road Mater Pavement Des 25:2729–2746. https://doi.org/10.1080/14680629.2024.2329457
24. Gong M, Sun Y, Chen J (2023) Effect of 3D aggregate shape on thermo-mechanical properties of asphalt concrete using a mesostructure-based homogenisation method. Int J Pavement Eng 24:2103129. https://doi.org/10.1080/10298436.2022.2103129
25. Kusumawardani DM, Wong YD (2021) Effect of aggregate shape properties on performance of porous asphalt mixture. J Mater Civ Eng 33:04021208. https://doi.org/10.1061/(ASCE)MT.1943-5533.0003801
26. Potyondy DO, Cundall PA (2004) A bonded-particle model for rock. Int J Rock Mech Min Sci 41:1329–1364. https://doi.org/10.1016/j.ijrmms.2004.09.011
27. Azevedo NM, Farinha MLB, Oliveira S (2024) Assessment of contact laws accounting for softening in 3D rigid concrete particle models. Buildings 14:801. https://doi.org/10.3390/buildings14030801
28. Azevedo NM, Farinha MLB, Oliveira S (2025) A novel 3D reinforced particle model for reinforced concrete fracture assessment: formulation and validation. Appl Mech 6:2. https://doi.org/10.3390/applmech6010002
29. Zhang L, Zheng G, Zhang K, Wang Y, Chen C, Zhao L, Xu J, Liu X, Wang L, Tan Y, Xing C (2022) Study on the extraction of CT images with non-uniform illumination for the microstructure of asphalt mixture. Materials 15:7364. https://doi.org/10.3390/ma15207364
30. Loz PHF, Angulo SC, Rebmann MS, Tutumluer E (2021) Use of a 3D structured-light scanner to determine volume, surface area, and shape of aggregates. J Mater Civ Eng 33:04021240. https://doi.org/10.1061/(ASCE)MT.1943-5533.0003824
31. Paixão A, Resende R, Fortunato E (2018) Photogrammetry for digital reconstruction of railway ballast particles–a

cost-efficient method. Constr Build Mater 191:963–976. https://doi.org/10.1016/j.conbuildmat.2018.10.048
32. Otsu N (1979) A threshold selection method from gray-level histograms. IEEE Trans Syst Man Cybern 9:62–66. https://doi.org/10.1109/TSMC.1979.4310076
33. Lu R, Luo Q, Wang T, Zhao C (2022) Comparison of clumps and rigid blocks in three-dimensional DEM simulations: curvature-based shape characterization. Comput Geotech 151:104991. https://doi.org/10.1016/j.compgeo.2022.104991
34. Ghazvinian E, Diederichs MS, Quey R (2014) 3D random Voronoi grain-based models for simulation of brittle rock damage and fabric-guided micro-fracturing. J Rock Mech Geotech Eng 6:506–521. https://doi.org/10.1016/j.jrmge.2014.09.001
35. Zhou W, Ji X, Ma G, Chen Y (2020) FDEM simulation of rocks with microstructure generated by Voronoi grain-based model with particle growth. Rock Mech Rock Eng 53:1909–1921. https://doi.org/10.1007/s00603-019-02014-0
36. Azevedo NM, Farinha MLB, Oliveira S (2022) A flexible particle model for rock fracture: validation and assessment of the influence of deformability on the macroscopic response. Geotechnics 2:523–548. https://doi.org/10.3390/geotechnics2030026
37. Azevedo NM, Lemos JV (2022) A hybrid particle/finite element model with surface roughness for stone masonry analysis. Appl Mech 3:608–627. https://doi.org/10.3390/applmech3020036
38. Ye Y, Thoeni K, Zeng Y, Buzzi O, Giacomini A (2019) A novel 3D clumped particle method to simulate the complex mechanical behavior of rock. Int J Rock Mech Min Sci 120:1–16. https://doi.org/10.1016/j.ijrmms.2019.06.002
39. Micaelo R, Al-Mansoori T, Garcia A (2016) Study of the mechanical properties and self-healing ability of asphalt mixture containing calcium-alginate capsules. Constr Build Mater 123:734–744. https://doi.org/10.1016/j.conbuildmat.2016.07.095
40. IPQ (2010) NP EN 13043:2004/AC:2010. Aggregates for bituminous mixtures and surface treatments for roads, airfields and other trafficked areas. Instituto Português da Qualidade, Caparica
41. Möller T, Trumbore B (1997) Fast, minimum storage ray-triangle intersection. J Graph Tools 2:21–28. https://doi.org/10.1080/10867651.1997.10487468
42. Mena-Chalco (2023) JP ray/triangle intersection. MATLAB central file exchange. https://www.mathworks.com/matlabcentral/fileexchange/25058-ray-triangle-intersection.
43. Krumbein WC (1941) Measurement and geological significance of shape and roundness of sedimentary particles. J Sediment Res 11: 64–72
44. Blott SJ, Pye K (2007) Particle shape: a review and new methods of characterization and classification. Sedimentology 55:31–63. https://doi.org/10.1111/j.1365-3091.2007.00892.x
45. IPQ (2002) NP EN 933-4:2002. In: Tests for geometrical properties of aggregates–part 4: determination of particle shape—shape index. Instituto Português da Qualidade, Caparica
46. IPQ (2002) NP EN 933-3:2002. In: Tests for geometrical properties of aggregates–part 3: determination of particle shape—flakiness index. Instituto Português da Qualidade, Caparica
47. Wadell H (1932) Volume, shape, and roundness of rock particles. J Geol 40:443–451. https://doi.org/10.1086/623964
48. Aschenbrenner BC (1956) A new method of expressing particle sphericity. J Sediment Res 26:15–31. https://doi.org/10.1306/74D704A7-2B21-11D7-8648000102C1865D
49. Câmara G, Micaelo R, Azevedo NM, Silva H (2024) Incremental viscoelastic damage contact models for asphalt mixture fracture assessment. Infrastructures 9:118. https://doi.org/10.3390/infrastructures9070118
50. Silva H (2005) Characterisation of the bituminous mastic and aggregate-mastic bond. Contribution to the study of bituminous mixtures' behaviour (in Portuguese). PhD thesis, University of Minho
51. Hunter AE, Airey GD, Collop AC (2004) Aggregate orientation and segregation in laboratory-compacted asphalt samples. Transp Res Rec 1891:8–15. https://doi.org/10.3141/1891-02
52. Skorych V, Dosta M (2022) Parallel CPU–GPU computing technique for discrete element method. Concurr Comput: Pract Exp 34:e6839. https://doi.org/10.1002/cpe.6839